Unconventional Resources 18 (2027) 100539

Contents lists available at ScienceDirect

Unconventional Resources

journal homepage: www.keaipublishing.com/en/journals/unconventional-resources/

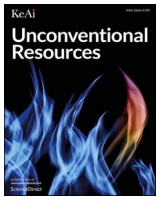

An explainable quantum neural network framework for reservoir permeability prediction from conventional well logs

Alvin K. Mulashani [a,*], Christopher N. Mkono [b,**], Melckzedeck M. Mgimba [a], Grant Charles Mwakipunda [c]

[a] Department of Geoscience and Mining Technology, College of Engineering and Technology, Mbeya University of Science and Technology, Box 131, Mbeya, Tanzania
[b] School of Marine Science and Engineering, South China University of Technology, Guangzhou, 511442, China
[c] Department of Civil and Environmental Engineering, College of Engineering, Qatar University, P.O. Box 2713, Doha, Qatar

ARTICLE INFO

Keywords:
Quantum neural network
Permeability
Well log
SHapley additive exPlanations

ABSTRACT

Accurate prediction of reservoir permeability is essential for reservoir characterization, production forecasting, and hydrocarbon recovery optimization. Conventional empirical and machine learning approaches often struggle to capture the complex nonlinear relationships between petrophysical variables while providing limited model interpretability. This study presents an explainable permeability prediction framework based on a variational Quantum Neural Network (QNN) simulated on classical hardware using the PennyLane quantum machine learning platform. The proposed framework integrates Shapley Additive Explanations (SHAP) to improve model transparency and facilitate geological interpretation of the learned relationships. A total of 3213 depth-matched samples acquired from three wells in the Mpyo Field, Albertine Graben, Uganda, were used to develop and evaluate the model using five conventional well-log measurements: thermal neutron porosity (TNPH), effective porosity (PHIE), formation density (RHOZ), spectral gamma ray (SGR), and shale volume (VSH). Hyperparameters of the QNN were optimized through systematic grid search and compared with a classical Group Method of Data Handling (GMDH), Random Forest (RF) and Support Vector Regression (SVR) models under identical experimental conditions. The simulated QNN achieved superior predictive accuracy, yielding training RMSE and MAE values of 0.019 and 0.0105, respectively, while demonstrating improved generalization on a blind test well compared with the benchmark model. SHAP analysis identified effective porosity as the dominant predictor of permeability, followed by thermal neutron porosity and spectral gamma ray, with feature contributions remaining consistent with established petrophysical principles. Bootstrap-based uncertainty analysis further demonstrated reliable prediction intervals across different reservoir intervals. Although implemented on a classical simulator rather than physical quantum hardware, the proposed framework illustrates the potential of quantum-inspired learning architectures for nonlinear permeability prediction while maintaining model interpretability for practical reservoir characterization.

1. Introduction

Energy is the most significant force behind global economic growth and development. The demand for energy rises in line with population growth and economic development. Over the last ten years, energy consumption has increased at an average annual rate of 1.9%, and this growth rate is expected to continue in the years to come [1,2]. The oil and gas sector, which contributes 6% of global GDP, faces mounting demands to reduce exploration risks and enhance recovery rates amid declining conventional reserves [3,4]. Understanding key petrophysical properties that control fluid storage and movement, accurately managing subsurface reservoirs efficiently. This can be concluded from the three main petrophysical properties (porosity, permeability, and hydrocarbon saturation), as they govern the accumulation, producibility, and overall quality of hydrocarbons within a reservoir. [3,4]. Permeability is one of the three properties that is the most crucial, because it

Peer review under the responsibility of KeAi Communications Co., Ltd.
* Corresponding author.
** Corresponding author.
E-mail addresses: alvin.mulashani@must.ac.tz (A.K. Mulashani), chrismkono@scut.edu.cn (C.N. Mkono).

https://doi.org/10.1016/j.uncres.2026.100539
Received 6 January 2026; Received in revised form 6 August 2026; Accepted 30 August 2026
Available online 31 August 2026
2666-5190/© 2026 The Authors. Publishing services by Elsevier B.V. on behalf of KeAi Communications Co. Ltd. This is an open access article under the CC BY-NC-ND license (http://creativecommons.org/licenses/by-nc-nd/4.0/).

determines how easy it is for fluids to flow through porous media and, as a result, has a significant impact on well production and recovery efficiency [5–8].

Traditional permeability estimation approaches rely heavily on laboratory-derived correlations, empirical relationships, or analytical models such as the Kozeny–Carman equation and Archie-based formulations [9–12]. Although widely used, these techniques are limited by oversimplified assumptions, scale inconsistencies, and difficulties in capturing the nonlinear interactions that arise in heterogeneous formations [13–15]. Moreover, core data are typically sparse, costly to acquire, and spatially discontinuous, necessitating the use of indirect measurements for continuous permeability profiling [5,16].

Well log measurements serve as an important part of the evaluation of reservoir parameters due to the continuous depth coverage provided by well logs, as well as their sensitivity to a variety of lithological, textural, and fluid-related variations [17]. Measurements of porosity, density, shale content, and gamma-ray response have been widely applied for the purpose of inferring trends in permeability, particularly in instances where high-density core data are not available [18,19]. However, the relationship between these logs and permeability tends to be complex and non-linear, and traditional regression-based methods do not typically reflect this level of complexity [20,21].

Machine Learning (ML) techniques are an alternative to traditional model development methods because of their capabilities to develop predictive models that incorporate multiple types of information and can be used to predict Nonlinear Relationships between independent and dependent variables, as well as to develop hybrid models that utilize Multiple Sources of Information [22,23]. In a review of the literature, different researchers have found that various ML techniques are currently being used to predict permeability for various reservoirs, and they include Boosted Trees, Kernel-based algorithms, Deep Learning, and Hybrid Optimization Frameworks [8,24–27].

Additionally, recent research on Explainable Artificial Intelligence (XAI) has highlighted the importance of developing models that are interpretable and understandable by end-users, particularly for subsurface decision making, which is critical in situations where there is a high degree of uncertainty or risk (Yang et al., 2025; Morales-Londoño et al., 2025). Remaining challenges related to the development of ML models remain, particularly with regard to the Generalizability, Interpretability, and Robustness of ML models when limited training datasets are available, and are drawn from a small number of well locations. A table provided (Table 1) details the advantages and limitations of the different ML techniques previously used to predict reservoir permeability.

Quantum machine learning, particularly Quantum Neural Networks (QNNs), has recently been explored as an alternative paradigm offering enhanced representational capacity through quantum-state encoding, entanglement, and high-dimensional feature mapping [34,35]. These characteristics suggest a potential advantage in modeling complex subsurface relationships that conventional ML models struggle to capture. It is important to note that the present implementation is a classically simulated QNN, the variational circuit is executed on conventional hardware using a quantum-circuit simulator, rather than on physical quantum processing hardware, consistent with the majority of current QNN studies in geoscience. Yet, their application to petrophysical permeability prediction remains limited, and comprehensive studies integrating QNN with interpretable frameworks are scarce.

To address these existing gaps, this study develops an explainable permeability prediction framework based on a simulated variational QNN implemented using PennyLane on classical hardware. The framework integrates SHAP to provide quantitative interpretation of feature importance and employs comprehensive statistical evaluation using blind-well testing, cross-validation, sensitivity analysis, and bootstrap-based uncertainty quantification. The proposed methodology is applied to 3213 well-log samples collected from three wells within the Mpyo Field of the Albertine Graben, Uganda.

The principal contributions of this study are fourfold: (i) the development of an explainable simulated QNN framework for permeability prediction from conventional well logs; (ii) quantitative interpretation of the learned relationships using SHAP together with geological analysis; (iii) rigorous evaluation of predictive robustness through cross-validation, sensitivity analysis, and uncertainty quantification; and (iv) a systematic comparison with established machine learning approaches to assess the practical potential and current limitations of simulated quantum learning for reservoir characterization. This balanced evaluation provides new insights into the role that quantum-inspired machine learning may play in future subsurface characterization workflows while recognizing the present technological constraints of quantum computing.

The remainder of this paper is structured as follows. Section 2 describes the geological setting and stratigraphy of the study area. Section 3 outlines the data preparation procedures and the methodological framework, including QNN architecture, GMDH, RF, SVR formulations, and the SHAP interpretability approach. Section 4 presents the model results, cross-validation analysis, uncertainty quantification, and feature-importance evaluation. Section 5 summarizes the main conclusions, highlights limitations, and provides considerations for future work.

Table 1
The permeability prediction models used previously, with their challenges.

Reference	Method Used	Challenges
[28]	Stacked extreme learning machine (ELM)	Time-consuming; Computationally expensive
[29]	Extreme gradient boosting (XGBoost)	Computationally expensive; Complex interpretability
[6]	Group method of data handling (GMDH)	Model complexity; Overfitting
[30]	Genetic algorithm (GA)	Prone to overfitting
[31]	Deep residual neural network (DRNN)	Prone to overfitting; Problem of gradient disappearance
[32]	Generalized additive model (GAM)	Prone to overfitting; Computationally expensive
[33]	Support vector machine (SVM)	Difficult to handle a large dataset
[5]	Multilayer perception with social ski-driver (MLP-SSD)	Slow convergence; Computationally expensive

2. Geological setting and lithostratigraphy

The Mpyo prospect is situated at the northern end of Lake Albert within Exploration Area 1 of the Albertine Graben, Uganda. The geological environment of the area is dominated by a fluvio-deltaic depositional system, significantly influenced by rapid fluctuations in lake levels [36,37]. Core data from nearby wells, particularly Well-1, confirmed the predominantly fluvial nature of the sandstone reservoirs, highlighting the prevalence of river-dominated depositional processes interspersed with occasional lacustrine flooding events. Upper Pliocene sandstone comprises the main reservoir units for the Mpyo Field and has been deposited in river-dominated distributary systems. Based on the correlation of logs from neighboring fields (Rii and Ngiri), the sand bodies have excellent lateral continuity and therefore, should provide good connectivity for fluid flow. The sandstone reservoirs range from medium to coarse-grained and are moderately sorted; there is also some variation in shale content depending on the distance to channel margins. Clay-rich layers intermittently deposited due to lacustrine flooding events serve as effective vertical baffles and seals [38,39]. The Location map of the Mpyo Block is shown in Fig. 1(a).

The trapping mechanisms in the Albertine Basin are primarily structural, associated with extensional tectonic forces that created the Albertine Rift during the Late Miocene. This tectonic activity resulted in a complex arrangement of fault blocks and relay ramps [40]. Hydrocarbon generation is associated with deeply buried, organic-rich

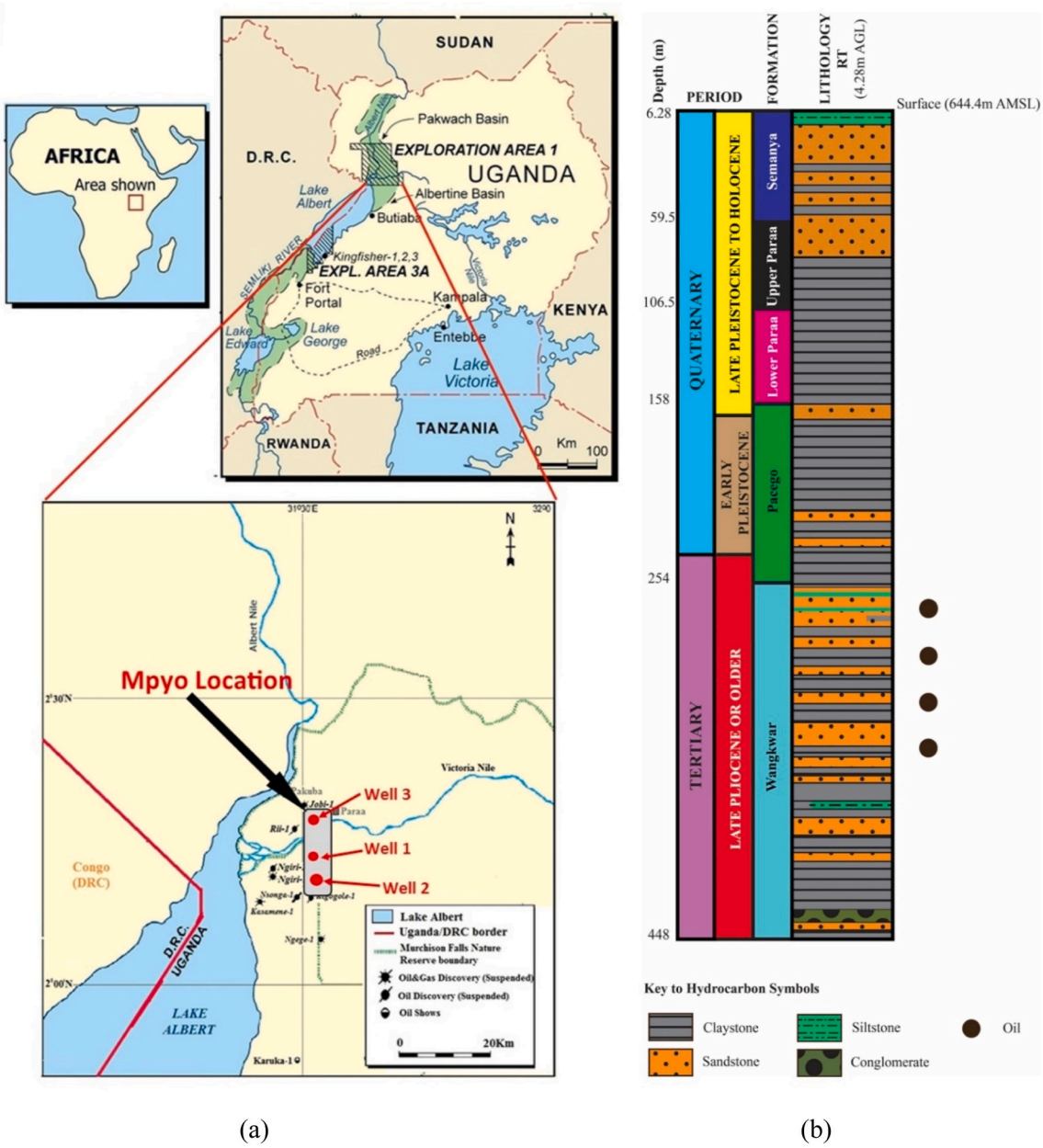

Fig. 1. (a) Location map of the Mpyo Block. (b) Stratigraphic diagram of the studied formations [3].

lacustrine shales of Miocene age, with migration occurring along fault conduits and through interconnected fluvial channel systems. Thick lacustrine mudstones deposited during high stand phases provide regional sealing capacity [41].

Regionally, the sedimentary fill above the basement is composed of Miocene to recent deposits, resting unconformably on the Precambrian basement. The stratigraphy of Mpyo well is based on outcrop data. The section is believed to be dominated by clastic sediments, predominantly Tertiary to Quaternary in age, with possible Pre-Tertiary clastic sediments overlying gneissose meta-sediments [42,43]. Climatically driven alternations between arid and humid intervals strongly influenced sediment supply and facies distribution, with sand-prone intervals corresponding to drier phases and clay-rich intervals corresponding to wetter conditions [44,45]. Fig. 1(b) shows the Stratigraphic diagram of the studied formations.

3. Methodology

3.1. Data handling and pre-processing

Data preprocessing techniques play a crucial role in enhancing the performance of machine learning models for reservoir permeability prediction [46,47]. The quality and quantity of well log data directly influence the upper limit of predictive accuracy, necessitating robust preprocessing methods to ensure reliable outcomes. Effective preprocessing involves several steps, including data cleaning, normalization, feature selection, and splitting datasets into training and testing subsets [48,49].

This study focused on three wells (Well-1, Well-2, and Well-3) situated in Uganda's Mpyo oilfield, specifically within the eastern section of Ondyek and the southern region of the Job East discovery. A combined total of 3213 samples were gathered from these wells, with 1462 from

Well-1, 799 from Well-2, and 952 from Well-3. The dataset included core permeability measurements and five well log parameters suit of thermal neutron porosity (TNPH), effective porosity (PHIE), standard resolution formation density (RHOZ), shale volume (VSH), and spectral gamma-ray (SGR).

To prevent information leakage, the dataset was first divided into the training wells and the independent blind test well. Feature normalization parameters were then calculated exclusively from the training dataset and subsequently applied to both the training and blind test datasets. This ensured that no information from the test data influenced model training or parameter estimation. All data underwent a systematic quality-control procedure that included the removal of non-physical values, depth-shift correction between logs and core plugs, and outlier detection was performed after data splitting using a z-score threshold of ±3 [50,51]. Missing values were addressed using univariate interpolation followed by cross-checking against adjacent log responses to ensure continuity in high-gradient intervals.

Core-analysis conditions were reviewed to ensure consistency across wells. Core plugs of 1 inch in diameter and 1.5–2 inches in length were measured at confining pressures of 1500–2000 psi under nitrogen flow at ambient laboratory temperature (≈22°C). Steady-state permeability measurements were preferred, and data exhibiting lamination-induced anisotropy or measurement instability were excluded.

Dataset partitioning followed a well-based split, where Well-1 and Well-2 were used for model training (70%), and Well-3 served as a blind test well (30%). This approach prevents cross-contamination of depth intervals and more realistically assesses model generalization to new wells. Five well log parameters, TNPH, RHOZ, SGR, VSH, and PHIE, were chosen as input variables for the model architecture, as depicted in Figs. 2 and 3. Statistical characteristics of these inputs are detailed in Table 2.

Data preprocessing technique, suppose there are N d-dimensional well log samples $(x_i, y_i), x_i \in R^d, y_i \in R^1$, where the input well log data x_i comprises corresponding output permeability data y_i. The permeability prediction input parameters exhibit different magnitudes and large differences in sample values. To make the scaled input features more interpretable, the d-dimensional well log input samples were normalized with values in the interval [0, 1], Equation (1).

$$\varphi_{in} = \frac{x_{im} - b_i}{a_i - b_i}, \tag{1}$$

Where, $b_i = \max x_i a_i = \min x_i i = 1, 2, \ldots\ldots, m,$ and $a_i = \min x_i b_i = \max x_i, i = 1, 2\ldots., m.$

3.2. Random Forest (RF)

RF is an ensemble learning technique widely applied in tasks like regression and classification. During training, it builds many decision trees, each contributing to the overall prediction of the data [52]. Moreover, it utilizes two key strategies: Bagging and Feature Randomness. These methods are responsible for its high accuracy, non-overfitting and capability to manage large data sets, which make it suitable for predictive analysis. In the Bagging method, each decision tree is trained with a different sample of the training data. In

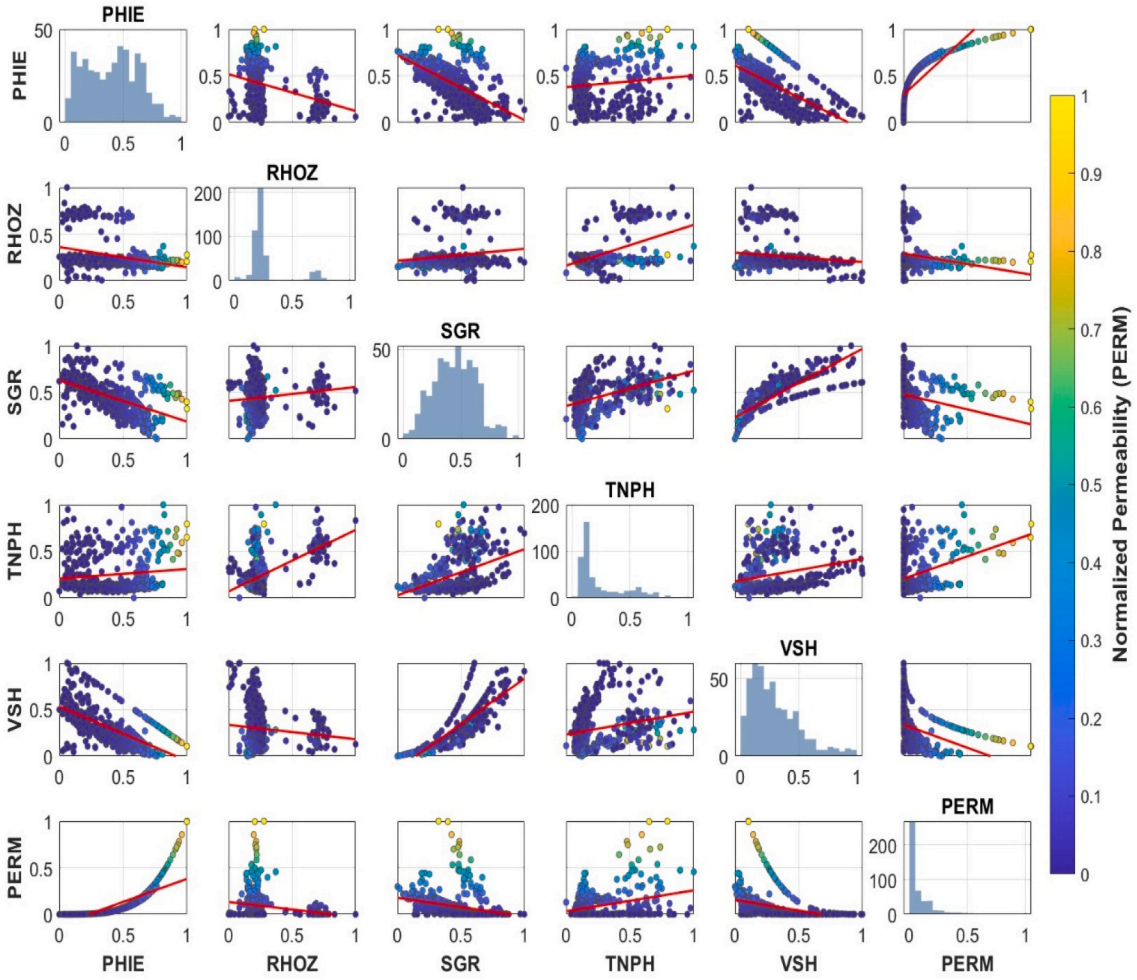

Fig. 2. Correlation analysis between input well log parameters and permeability.

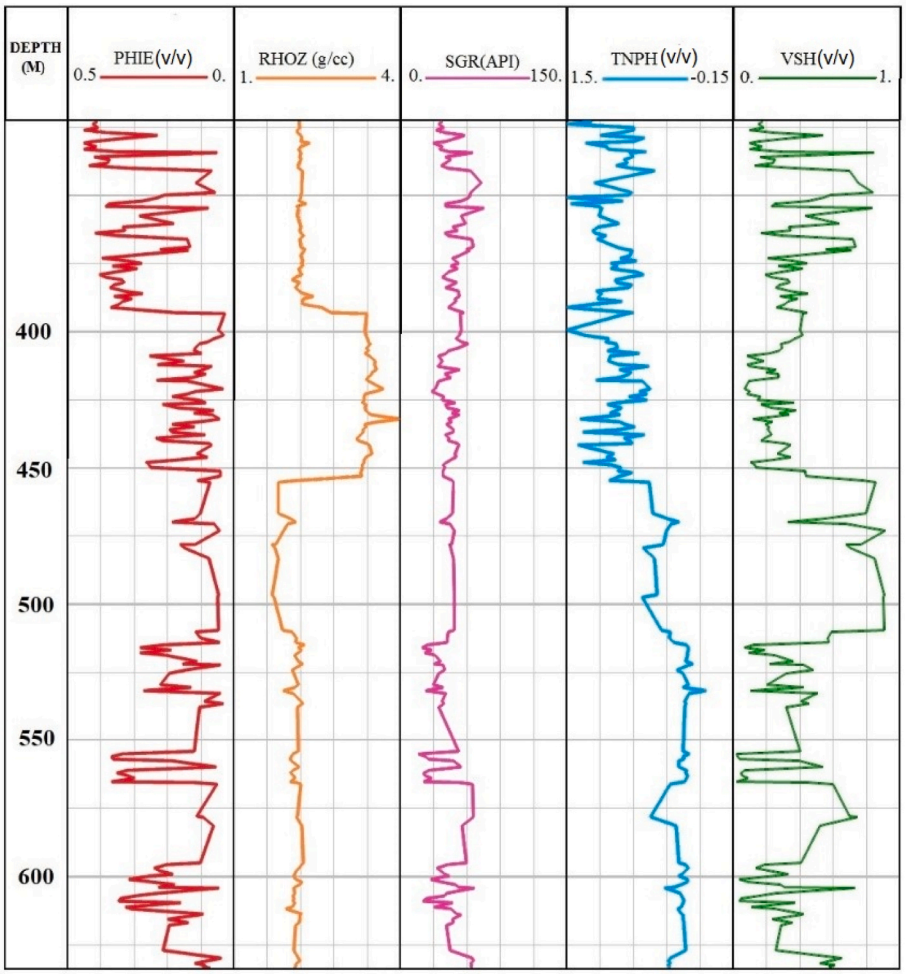

Fig. 3. Geophysical well logs suite of thermal neutron porosity (TNPH), rock's shale volume (VSH), (RHOZ), natural gamma ray (SGR), and limited effective porosity (PHIE).

determining splits at each node, a random selection of features is used so that each tree sees a different set of variables. This means increased tree diversity and decreased tree correlation leading to a stronger model. This will make the decision tree trained by RF rely on different data subsets, and use different feature sets for making decisions [53].

3.3. Support Vector Regression (SVR)

Support vector regression (SVR) is a powerful supervised learning algorithm that is commonly used to solve nonlinear regression problems. The goal of SVR is to find a function that can accurately predict the continuous target, without compromising the model's generalizability [54]. The algorithm searches for a regression function that fits into a specified maximum error (epsilon-insensitive tube) below the specified maximum error. SVR is designed to minimize the model complexity while simultaneously reducing prediction errors. The optimization process aims to minimize the distance from the data points and to minimize the slope of the regression surface [55]. The data points that fall below or above the epsilon-insensitive region are called as support vectors, and they are used to determine the regression function to a large extent. For datasets with nonlinear relationships, SVR can incorporate kernel functions such as the radial basis function (RBF), polynomial, or sigmoid kernels to map the input variables into a higher-dimensional feature space. The ability to represent complex, nonlinear patterns more effectively in this transformed space can help SVR model more accurately complex relationships between the input features and the target variable, which can enhance the accuracy of its predictions.

3.4. Group Method Data Handling (GMDH)

The GMDH neural network delivers significant benefits across diverse fields [56,57]. Its resilience and flexibility enable it to manage intricate, nonlinear, and noisy datasets effectively, proving applicable to many domains. A standout feature is its ability to autonomously select models, which avoids the need for pre-established architectures. By systematically creating and assessing models, it identifies the best-performing solution while minimizing the chance of overfitting [58]. Furthermore, the network's transparency enhances comprehension of connections between inputs and outputs, supporting data-driven decisions. Scalability is another strength, as it manages extensive datasets efficiently via parallel computing, positioning it as ideal for big data tasks and real-time analytics. Finally, its inductive approach and stepwise model-building method shorten training periods, enabling quicker model creation and implementation, which boosts productivity.

The GMDH neural network excels in predictive tasks due to its capacity to process vast and intricate data while independently identifying key features [59]. When applied to permeability data from well logs, it can recognize underlying patterns and correlations, forming the basis for generating precise forecasts. GMDH implementations rely on polynomial reference functions. For instance, Volterra's series functions, the discrete equivalent of the Kolmogorov-Gabor polynomial, can define the general relationship between input and output variables, equation (2)

Table 2
Statistical characteristics of the used data.

Wells	Well log	Statistical features				
		Minimum	Maximum	Average	Standard Deviation	Range
Well 1	TNPH (v/v)	0.123	1.616	0.741	0.348	1.492
	SGR (API)	16.212	74.875	44.568	11.207	58.663
	VSH (pU)	0.02	0.912	0.346	0.219	0.892
	PHIE (%)	0.009	0.372	0.188	0.099	0.363
	RHOZ (g/cc)	1.683	4.097	2.481	0.587	2.414
Well 2	TNPH (v/v)	0.123	1.615	0.494	0.311	0.382
	SGR (API)	8.425	74.87	38.18	12.13	27.58
	VSH (pU)	0.0016	0.912	0.268	0.191	0.425
	PHIE (%)	0.017	0.451	0.195	0.099	0.25
	RHOZ (g/cc)	1.683	4.097	2.338	0.41	1.83
Well 3	TNPH (v/v)	0.252	1.035	0.376	0.101	0.783
	SGR (API)	13.699	72.729	42.145	15.535	59.03
	VSH (pU)	0.014	0.911	0.309	0.24	0.897
	PHIE (%)	0.009	0.372	0.188	0.098	0.363
	RHOZ (g/cc)	1.927	3.486	2.169	0.128	1.559

[11,58]

$$\omega = a_0 + \sum_{i=1}^{n} a_1 x_i + \sum_{i=1}^{n}\sum_{j=1}^{n} a_{2j} x_i x_j + \sum_{i=1}^{n}\sum_{j=1}^{n}\sum_{k=1}^{n} a_{3jk} x_i x_j x_k + \ldots \quad (2)$$

where $\{x_1, x_2, x_3 \ldots\}$ represents the inputs, $\{a_0, a_1, a_2, a_3 \ldots\}$ are the coefficients of the polynomial, and ω is the output node. The above discrete polynomial equation (3) can be expressed by the following system of partial quadratic polynomials, which contains only two neurons as follows, GMDH algorithm Flowchart is shown in Fig. 4.

$$\widehat{\omega} = a_0 + a_1 x_i + a_2 x_j + a_3 {x_i}^2 + a_4 {x_j}^2 + a_5 x_i x_j \quad (3)$$

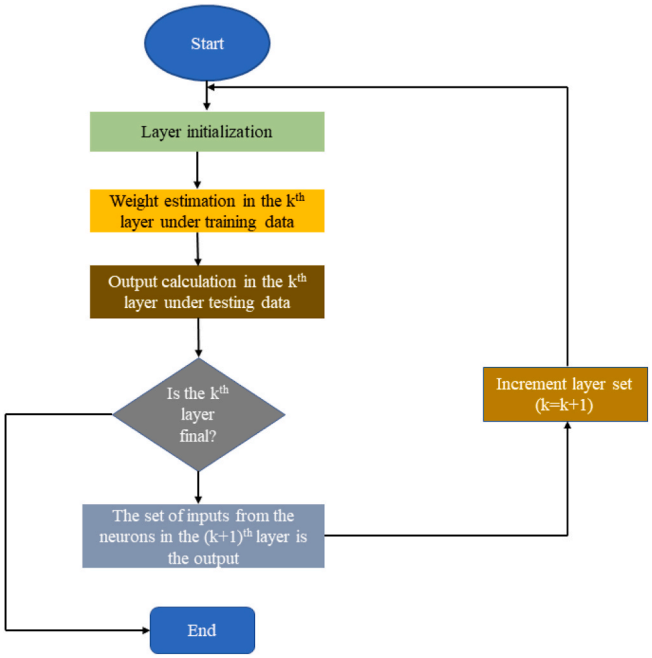

Fig. 4. GMDH algorithm flowchart [2].

3.5. Quantum neural network

The Quantum Neural Network (QNN) used in this study provides a new direction in supervising both the popular classical and a Quantum Kernel in the prediction of reservoir permeability [34]. Due to the presence of quantum gates in this architecture, solving the problem of strength prediction is expected to be achieved through the proposed 2 hidden layers. Quantum gates mainly work with linear superposition and entanglement, which serve as the main points needed for neurons to define high-level features and enhance their combination efficiently, in which all the gates are interconnected to Q-bits needed to make a training process. The true mechanism of neurons along those gates integrates both quantum-based principles, which are more efficient in representing and sharing information than in a standard basis. The quantum neural network comprises output neuron *m,* hidden neurons, and *n* input neurons, as shown in Fig. 5.

Thus, the input x_i, of datasets $(x_i, y_i), x_i \in R^d, y_i \in R^1$, is pre-processed in the interval $[0, 1]$ and encoded into the input state of the quantum neural network [35]. The first layer converts them to quantum states Φ_{ij}; thus, their phase values (Equation (4)) lie in the interval $\left[0, \frac{\pi}{2}\right]$.

$$\Phi ij = \frac{\pi}{2}\varphi_{in} \quad (4)$$

The hidden layer receives the output value pertaining to the quantum neuron of the first layer, and the output of the *j-th* quantum neuron of the hidden layer (equation (5)), which becomes the second layer [34].

$$h_j = \sin\left(\frac{\pi}{2} f(\alpha_j) - \beta_j\right), \quad (5)$$

The quantum transition position that determines the shapes of quantum intervals, which represent adjustable parameters of the quantum neural network denoted by β_j, The reversal parameter is denoted by α_j, and the activation function of the hidden layer, specified in equation (7) below, is denoted $g(x)$; the model learns and adjusts the associated weight and translation parameters (α_j, β_j) to attain the optimal value [60,61].

The output of the input layer neurons can be obtained as equation (6) in the third layer, this layer performs a weighted summation of the output h_j of the hidden layer.

$$\widehat{y}_k = g(W_{kj} h_j) \quad (6)$$

Where the connection power pertaining to the quantum neuron situated in the hidden layer is w_{jk} , the chosen output function is *g*, and the actual output of the quantum neural network is denoted by $\widehat{y}_k$. Since the wavelet function exhibits satisfactory time frequency localization characteristics and satisfactory resolution of the logging signal in both the time and frequency domains, it is utilized as the activation function (Equation. (7)), herein denoted as QNN_W, for the hidden layer of the quantum neural network; furthermore, the sigmoid function (Equation. (8)), herein denoted as QNN_S, is utilized for the output layer [35,62].

$$g(x) = \frac{\cos 1.75\, x}{e^{\frac{x^2}{2}}}, \quad (7)$$

$$f(x) = \frac{1}{1 + e^{-x}}. \quad (8)$$

Assume there are *N* d-dimensional fluid observation samples, (x_i, y_i), $x_i \in R^d, y_i \in R^1, Y = (y_1, y_2, \ldots . y_N)$ where is the actual output, $\widehat{y} = (\widehat{y}_1, \widehat{y}_2, \widehat{y}_3, \ldots . , \widehat{y}_N)$ is the desired output, and the loss function is the mean

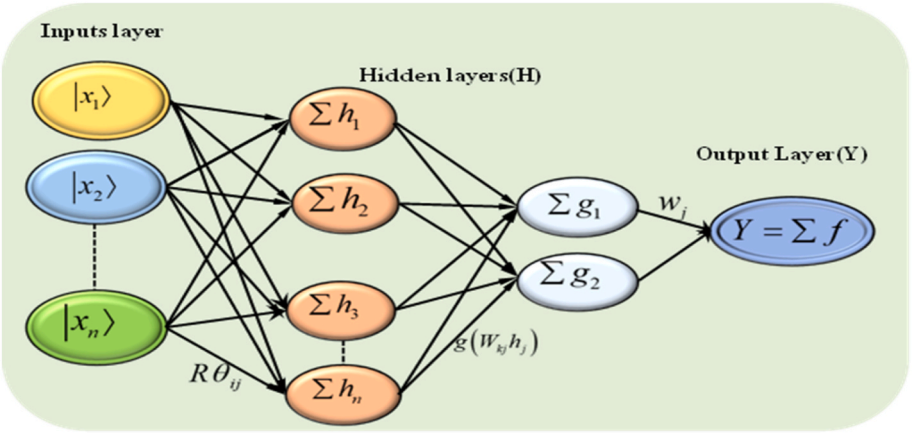

Fig. 5. Quantum neural network structure.

squared error (RMSE) in equation (9) and mean absolute error (MAE) in equation (10).

$$RMSE = \sqrt{\frac{1}{m}\sum_{i=1}^{m}(\hat{y}_i - y_i)^2} \tag{9}$$

$$MPIW = \frac{1}{N}\sum_{i=1}^{N}(U_i - L_i) \tag{10}$$

Reducing the loss function is essentially an optimization task. The objective of the learning process is to decrease the root mean square error by adjusting the parameters of the network. When the gradient descent algorithm is used to update the parameters $\theta_{ij}, \alpha_j, w_{jk}$ and β_j of the quantum neural network, the update rule for θ_{ij} can be expressed as:

$$\theta_{ij}(t+1) = \theta_{ij}(t) + \gamma\Delta\theta_{ij}(t) \tag{11}$$

$$\Delta\theta_{ij} = \frac{\partial E}{\partial\theta_{ij}} = \sum_{k=1}^{m}(\hat{y}k - yk)g'(w_{jk}h_j)w_{jk}\cos\left(\frac{\pi}{2}f(\alpha_j) - \beta_j\right)\frac{T_{ij}}{1+S_j^2}, \tag{12}$$

$$T_{ij} = \frac{\cos(\varphi_{in}+\theta_{ij})S_{j1} + \sin^2(\varphi_{in}+\theta_{ij})}{S_{j1}^2}, \tag{13}$$

$$S_j = \frac{\sum_i^n = 1^{\sin}(\varphi_{in}+\theta_{ij})}{\sum_i^n = 1^{\cos}(\varphi_{in}+\theta_{ij})}, \tag{14}$$

$$S_j = \sum_{i=1}^{n}\cos(\varphi_{in}+\theta_{ij}). \tag{15}$$

The update formula for α_j can be expressed as

$$\alpha_j(t+1) = \alpha_j(t) + \gamma\Delta\alpha_j(t), \tag{16}$$

$$\Delta\alpha_j = \frac{\partial E}{\partial\alpha_j} = -\frac{\pi}{2}\sum_{k=1}^{m}(\hat{y}k - yk)g'(w_{jk}h_j)w_{jk}\cos\left(\frac{\pi}{2}f(\alpha_j) - \beta_j\right)f'(\alpha_j) \tag{17}$$

The update formula for w_{jk} can be expressed as

$$w_{jk}(t+1) = w_{jk}(t) + \gamma\Delta w_{jk}(t), \tag{18}$$

$$\Delta w_{jk} = -\frac{\partial E}{\partial w_{jk}} = -(\hat{y}k - yk)g'\sin\left(\frac{\pi}{2}f(\alpha_j) - \beta_j\right), \tag{19}$$

The update formula for β_j can be expressed as

$$\beta_j(t+1) = \beta_j(t) + \gamma\Delta\beta_j(t), \tag{20}$$

$$\Delta\beta_j = \frac{\partial E}{\partial\beta_j} = \sum_{k=1}^{m}(\hat{y}k - yk)g'(w_{jk}h_j)w_{jk}\cos\left(\frac{\pi}{2}f(\alpha_j) - \beta_j\right) \tag{21}$$

Where γ denotes the learning efficiency.

3.6. Blocked five-fold cross-validation

This study used blocked five-fold cross-validation (CV) instead of the standard random k-fold CV to reduce optimistic bias from well log measurements that are correlated along the well path depth to get more realistic measures of generalization. There is a high degree of vertical continuity in well log data, and it is possible that if adjacent depth samples were randomly assigned to different folds that this could lead to information leakage as adjacent samples may have similar petrophysical properties. This leakage can present spurious accuracy and result in unrealistic estimates of predictive accuracy.

To overcome this, the training data set was divided into five contiguous blocks of data of roughly equal thickness, each of which was used as an independent validation data set (Table 6). In each iteration, one full depth interval was reserved for validation and the remaining four were used for training the model. This process was repeated until all the depth blocks were used one time as the validation set. The blocked strategy maintains the spatial continuity of the reservoir and more accurately represents the practical reservoir characterization problem, in which permeability predictions are desired for areas that have not been previously observed.

Blocked cross-validation was used during model development for hyperparameter tuning and model selection. Following the identification of the optimum model configuration, the final QNN, GMDH, RF and SVR models were retrained with the full training set and then tested using an independent blind test well. This two-stage validation approach offers a comprehensive assessment of the within-well generalization to other continuous depth intervals as well as between-well predictive performance.

3.7. Global sensitivity analysis

A global sensitivity analysis was conducted to assess the relative importance of each input feature in influencing the predicted permeability values. The cosine-amplitude sensitivity index (CASI) was adopted as the primary sensitivity technique because it is computationally efficient and capable of capturing nonlinear dependencies between inputs and outputs [63].

Prior to analysis, all predictor variables were normalized to remove unit effects and to ensure uniform scaling across the feature space. CASI was then computed by measuring the cosine of the angle between each input vector and the permeability output vector in a normalized multidimensional space. This metric provides a scalar value reflecting the degree of alignment between each predictor and the modeled target. Equation (22) was used to compute the value of CASI.

$$CASI = \frac{\sum A_i * B_i}{\sqrt{\sum A_i^2 * \sum B_i^2}} \quad (22)$$

Where A and B are pairs of datasets. The CASI procedure was applied to the five petrophysical logs used as input features in the QNN and GMDH models. The resulting sensitivity values were subsequently compared with SHAP-derived feature importance scores during the results phase to ensure consistency between global and local interpretability methods.

3.8. Uncertainty quantification

Uncertainty Quantification (UQ) was performed to characterize the confidence associated with QNN-based permeability predictions and to provide interval estimates rather than single deterministic outputs. A bootstrap resampling technique was selected for UQ because it does not require parametric assumptions and is well suited to datasets with potentially complex statistical structures [64].

A total of 500 bootstrap replicates were generated by sampling the training dataset with replacement. For each replicate, the QNN was retrained using the same optimized hyperparameters that were identified during the main training phase. The retraining procedure produced a unique permeability model for each bootstrap sample, allowing a distribution of predictions to be generated at each depth point in the test well. Prediction intervals were then computed from these distributions by extracting the 2.5th and 97.5th percentiles, forming a 95% prediction interval (U95). The width of these intervals was used as a quantitative indicator of prediction uncertainty. This UQ procedure provides insight into the reliability of QNN predictions and enables identification of depth intervals where geological heterogeneity or log-response variability may contribute to increased predictive uncertainty.

4. Results and discussion

4.1. Parameter settings and QNN model development

To improve reservoir permeability prediction accuracy, the quantum neural network is presented, with Shapley additive explanation values for the explanation of individual permeability prediction results. A structured hyperparameter tuning strategy was employed for both models to ensure a fair and consistent comparison. A systematic grid-search procedure was used to explore the key hyperparameters for each model. For the QNN, the tuning process evaluated learning rates in the range of 0.001-0.05, batch sizes from 8 to 64, optimizer types (Adam, RMSprop, and SGD), the number of variational layers (1-4), and circuit ansatz configurations differing in entanglement connectivity as shown in Table 3.

Table 3
Hyperparameter tuning results for QNN.

Hyperparameter	Tested Range	Optimal Value	Description
Number of Qubits	2, 4, 6, and 8	4	Controls the dimension of the quantum feature space
Quantum Layers	1, 2, 3	2	Depth of quantum circuit impacting expressiveness
Learning Rate	0.001, 0.01, 0.05, 0.1	0.01	Step size used by the optimizer
Optimizer	Adam, SGD, RMSprop	Adam	Affects convergence speed and stability
Batch Size	8, 16, 32, 64	32	Number of samples used per gradient update
Circuit Ansatz	Hardware-Efficient, Strongly Entangling	Hardware-Efficient	Impacts expressiveness and trainability
Number of Epochs	50, 100, 200	100	Total passes over the dataset

Hyperparameter selection was performed using blocked five-fold cross-validation, in which the training data were partitioned into five contiguous depth intervals of approximately equal thickness. During each iteration, one complete depth block was reserved for validation while the remaining four blocks were used for model training. This strategy preserves the spatial continuity of the well-log measurements and minimizes information leakage arising from depth autocorrelation, thereby providing a more realistic assessment of model generalization. The hyperparameter combination producing the lowest average validation error across the five depth blocks was selected as the optimal configuration. After optimization, the final QNN, GMDH, RF, and SVR models were retrained using the complete training dataset and subsequently evaluated on the independent blind test well.

To control overfitting, early stopping based on validation-loss convergence was employed during QNN training, while model complexity in the GMDH network was controlled through an external validation criterion that automatically terminated layer expansion when no further improvement in prediction accuracy was achieved. The RF and SVR models were similarly regularized through optimization of their respective complexity parameters during the grid-search process.

All computational experiments were conducted in Python (version 3.12.3). The simulated QNN was implemented using PennyLane (version 0.38.0), an open-source quantum machine-learning framework. Quantum operations were simulated using PennyLane's default.qubit simulator, which employs Python and Autograd on classical hardware. The QNN simulations were executed on a system equipped with an NVIDIA GeForce RTX™ 4050 Laptop GPU and a 13th Gen Intel® Core™ i9-13900H CPU. This unified computational environment ensured consistent execution and equitable resource allocation across all tested models.

The QNN circuit, showing three main stages of quantum operations applied to four qubits, is shown in Fig. 6. In the first stage (top panel), Hadamard (H) gates are applied to each qubit to create a superposition, followed by parameterized phase shift (P) gates encoding the input data *x[i]*. Controlled-NOT (CNOT) gates then introduce entanglement between qubits, enabling correlation of quantum states. Additional multi-qubit entangling operations with phase shift gates parameterized by functions of $(\pi - x[i])$ further capture complex dependencies among features, forming the data encoding block of the QNN.

In the second and third stages (middle and bottom panels), the circuit applies trainable variational layers designed to learn patterns from the encoded well logs data. These layers consist of controlled operations interleaved with parameterized $RY(\theta)$ rotation gates, where θ are the trainable weights updated during optimization. The controlled gates maintain entanglement, while the rotations adjust the probability amplitudes to fit the training well log data. The depth of the circuit with entanglement layers and rotation gates reflects its capacity to model complex relationships between well log and permeability.

The results show that the QNN permeability model's predictive performance is highly sensitive to the careful balancing of circuit expressiveness and optimization stability (Table 3). The most influential parameters are the number of qubits and quantum layers, as they determine the model's capacity to capture complex permeability patterns, too few limits learning, too many increases noise and optimization difficulty. The optimal settings found were 4 qubits and 2 layers, combined with a hardware-efficient ansatz to reduce gate count and noise while retaining sufficient correlation capture.

4.2. Performance indicators and error analysis of reservoir permeability

The predictive permeability models were evaluated and compared using statistical indicators, namely the correlation coefficient (R), mean absolute error (MAE), and relative root mean square error (RMSE). A correlation coefficient (R) value approaching 1 indicates optimal model performance, whereas MAE and RMSE values approaching zero suggest

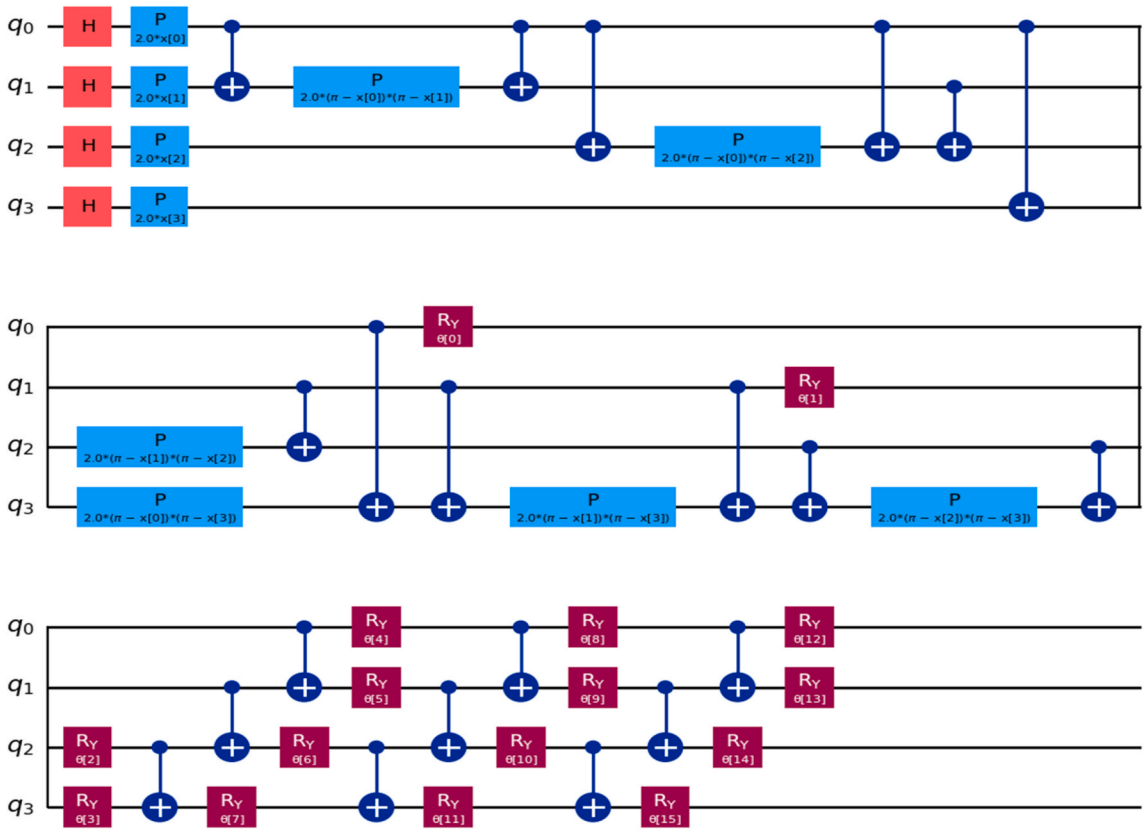

Fig. 6. QNN circuit, with four qubits.

that the model serves as a reliable predictor. The mathematical formulations for R, MAE, and RMSE are presented in Equations (23)–(25) [2, 3].

$$R = \frac{\sum_{i=1}^{N}(y_i - \bar{y})(Y_i - \bar{Y}_i)}{\left(\sqrt{\sum_{i=1}^{N}(y_i - \bar{y}_i)^2}\right)\left(\sqrt{\sum_{i=1}^{N}(Y_i - \bar{Y}_i)^2}\right)} \tag{23}$$

$$MAE = \frac{1}{N}\sum_{i=1}^{n}|y_i - Y_i| \tag{24}$$

$$RMSE = \sqrt{\left(\frac{1}{N}\sum_{i=1}^{N}(y_i - Y_i)^2\right)} \tag{25}$$

Here, N denotes the total number of data points, y_i represents the measured parameter value, $\bar{Y}_i$ is the mean of the predicted parameters, $\bar{y}_i$ is the mean of the measured parameters, and Y_i denotes the estimated parameter value [65]. During training, MAE and RMSE values approaching zero indicate better model fitting. However, greater importance is given to the model's performance on the withheld testing dataset. Thus, when the testing MAE and RMSE values approach zero, it signifies a superior model with enhanced generalization capability [66, 67].

The development of permeability models involved analyzing a range of factors and dynamic development aspects impacting permeability based on the well log dataset, utilizing SHapley Additive exPlanations (SHAP). The QNN permeability model outperformed the GMDH, RF and SVR permeability model in the evaluations. Specifically, the QNN model displayed superior performance, showcasing the lowest error rates with a Root Mean Squared Error (RMSE) of 0.019 and Mean Absolute Error (MAE) of 0.0105 during training. Conversely, the GMDH model exhibited RMSE and MAE values of 0.044 and 0.0903. In comparison, the ensemble and kernel-based benchmark models demonstrated higher training error rates, with RF achieving an RMSE of 0.068 and MAE of 0.0451, while SVR produced the highest training errors across all models with an RMSE of 0.0952 and a MAE of 0.0628, as indicated in Table 4 and Fig. 7. This hierarchy during the training phase further underscores the superior fitting capacity and expressive power of the QNN architecture prior to testing on unseen data.

To assess the models' ability to generalize, they were tested on unseen well log data from well 3, which was not part of the data used to develop the models, enabling an unbiased evaluation of performance with new input well log data. The tested QNN-based permeability model was identified as the most effective, producing predictions that closely matched the actual permeability measurements. As illustrated in Fig. 7, the QNN achieved the lowest error rates, with an RMSE of 0.1162 and an MAE of 0.0725. In comparison, the GMDH model yielded higher error values, with an RMSE of 0.2257 and MAE of 0.1482, while the RF had RMSE of 0.3155 and MAE of 0.2103 and SVR had RMSE of 0.4126 and MAE of 0.2850 as shown in Table 4 and Fig. 7.

The lower RMSE and MAE values from the QNN suggest minimal deviation between predicted and actual permeability values. Consequently, the testing RMSE value of 0.1162 confirms that the proposed

Table 4
Permeability predictive models' statistical measures.

Model	Training		Testing	
	RMSE	MAE	RMSE	MAE
QNN	0.019	0.0105	0.1162	0.0725
GMDH	0.0440	0.0903	0.2257	0.1482
RF	0.0680	0.0451	0.3155	0.2103
SVR	0.0952	0.0628	0.4126	0.2850

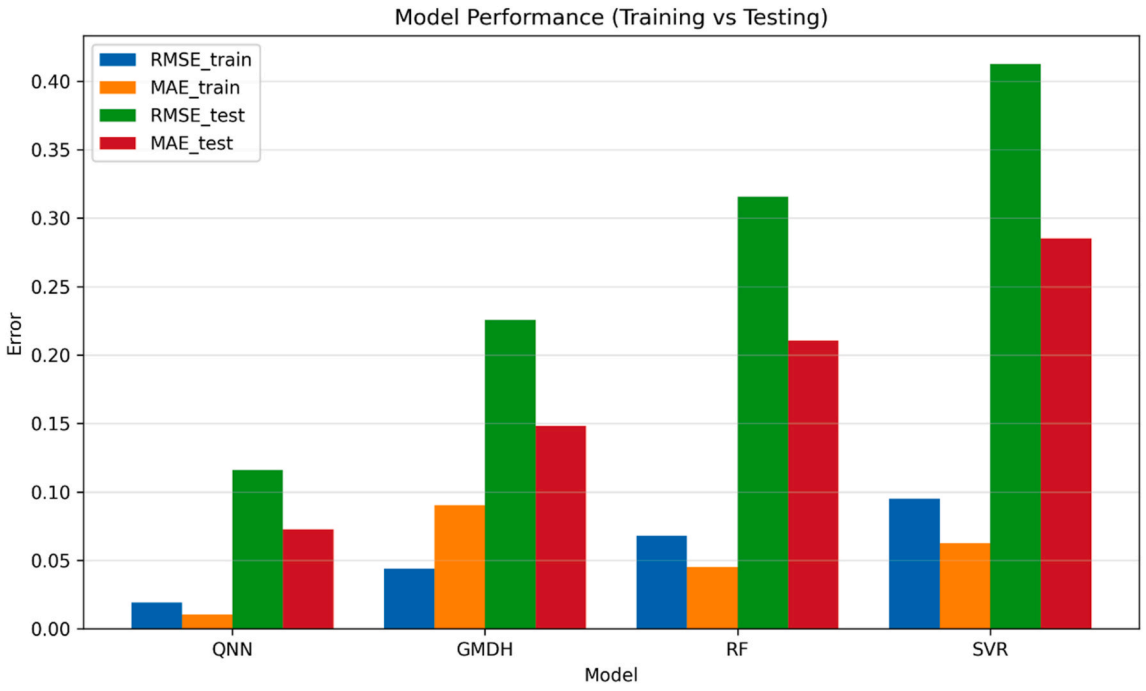

Fig. 7. RMSE and MAE error analysis for QNN, GMDH, RF and SVR during permeability prediction.

model outperforms other models in terms of both accuracy and stability (Fig. 8).

The QNN-based permeability model achieved the highest R values of 0.998 for training and 0.953 for testing, as illustrated in Table 5 and Fig. 9 (a) and Fig. 10 (a). This indicates that QNN explains about 2% more variance in the testing phase and consistently captures the underlying relationship between well log input features and Reservoir permeability, while also generalizing well to unseen well log data more

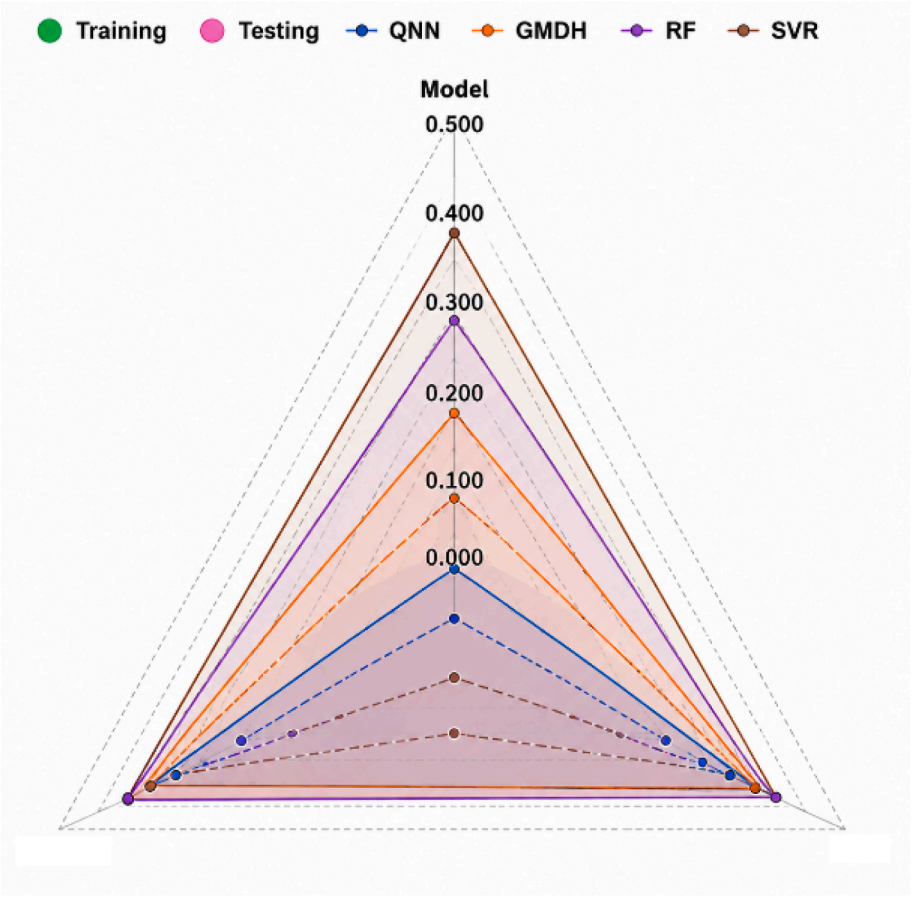

Fig. 8. Radar plot of model accuracy across QNN, GMDH, RF and SVR Models.

Table 5
The comparative summary of training and testing performance.

Model	Training		Testing	
	R	Key Insight	R	Key Insights
QNN	0.998	Outstanding fit with nearly perfect prediction; well-tuned quantum circuit enhanced performance	0.953	Excellent generalization; consistent and reliable performance
GMDH	0.965	Strong accuracy; good nonlinear mapping with minor deviations	0.937	Good predictive strength; minor drop from training accuracy
RF	0.902	Good predictive capability; ensemble learning effectively captures overall permeability trends but with noticeable deviations from measured values	0.881	Moderate generalization performance; increased prediction dispersion, particularly for high-permeability samples
SVR	0.875	Acceptable nonlinear prediction; captures the general trend but exhibits larger errors and reduced sensitivity to complex permeability variations	0.846	Fair generalization; largest performance degradation and weakest agreement with measured permeability among the evaluated models

effectively. In comparison, the GMDH permeability model recorded slightly lower R values of 0.965 for training and 0.937 for testing, suggesting marginally reduced predictive accuracy as shown in Table 5 and Figs. 9(b) and 10(b). The RF model exhibited intermediate predictive performance, with training and testing correlation coefficients of 0.902 and 0.881, respectively (Fig. 9(c) and 10(c)). Although the RF model successfully captured the overall permeability trend, a greater dispersion of data points around the 1:1 reference line was observed, particularly at moderate-to-high permeability values, indicating increased prediction errors compared with both QNN and GMDH. The SVR model produced the lowest predictive performance among the four models, yielding R values of 0.875 for training and 0.846 for testing (Fig. 9(d) and 10(d)). The corresponding cross-plots reveal a wider scatter around the ideal agreement line and a noticeable tendency to underestimate high-permeability samples while overestimating some low-permeability values, reflecting its comparatively weaker ability to model the highly nonlinear characteristics of the permeability dataset. Overall, the predictive performance follows the order QNN > GMDH > RF > SVR, confirming that the quantum neural network provides the most accurate and robust permeability predictions for both the training and testing datasets.

The QNN's training process adaptively discovers which input well log features and interactions most strongly govern permeability, and it refines its internal architecture to emphasize those dominant relationships. As the model iterates, it prunes or suppresses neurons that do not materially reduce prediction error, effectively simplifying itself while preserving predictive power. QNN points cluster more tightly around the line across ranges, with narrower residual distributions, whereas GMDH shows wider scatter and larger bias in the low end and growing dispersion at high values as illustrated in Fig. 11. The RF model displays an even wider residual distribution than GMDH, with more pronounced tails extending away from zero, indicating a larger spread of prediction errors and reduced consistency across the dataset. Similarly, the SVR model presents the broadest and flattest residual distribution among all the evaluated models, reflecting the highest prediction variance and the greatest occurrence of large positive and negative residuals. The broader residual profiles of both RF and SVR are consistent with their lower correlation coefficients and the increased dispersion observed in the cross-plots, demonstrating their comparatively weaker capability to capture the highly nonlinear relationship between well log responses and reservoir permeability. This combination of automatic architecture optimization, effective feature selection, and principled pruning is what underpins QNN's stronger alignment with the measured data.

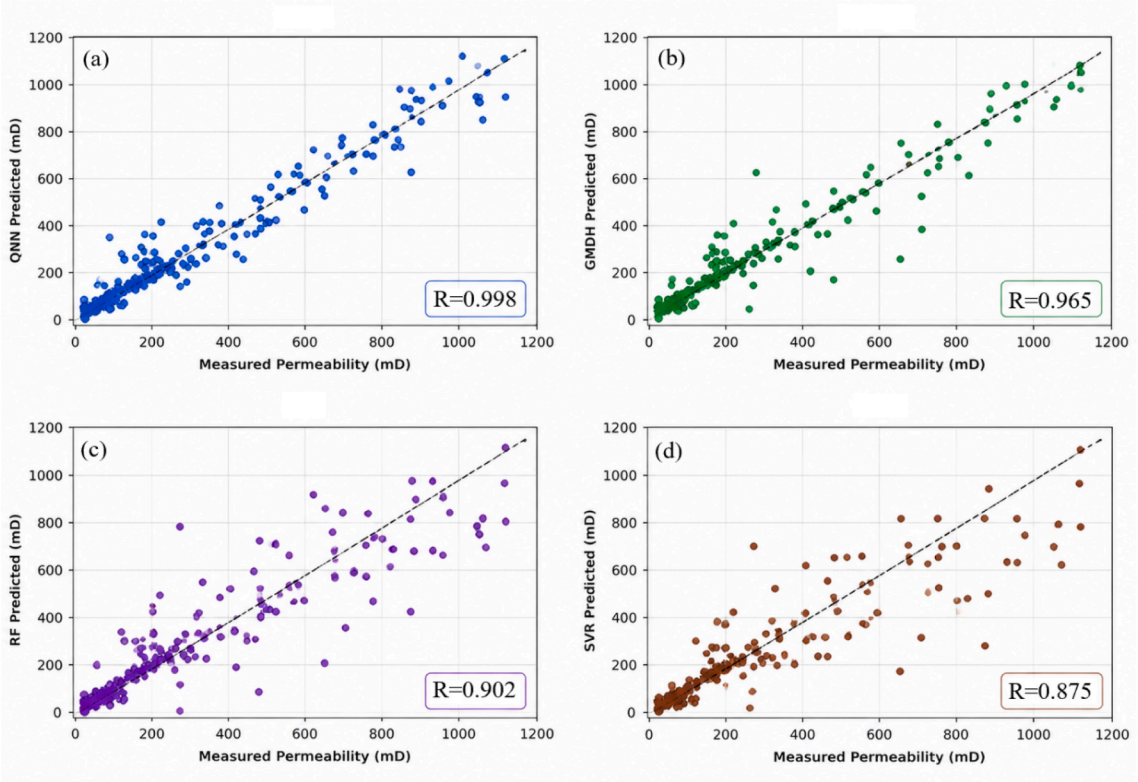

Fig. 9. Comparison between measured and predicted permeability (mD) values during the training phase (a) QNN, (b) GMDH, (c) RF and (d) SVR.

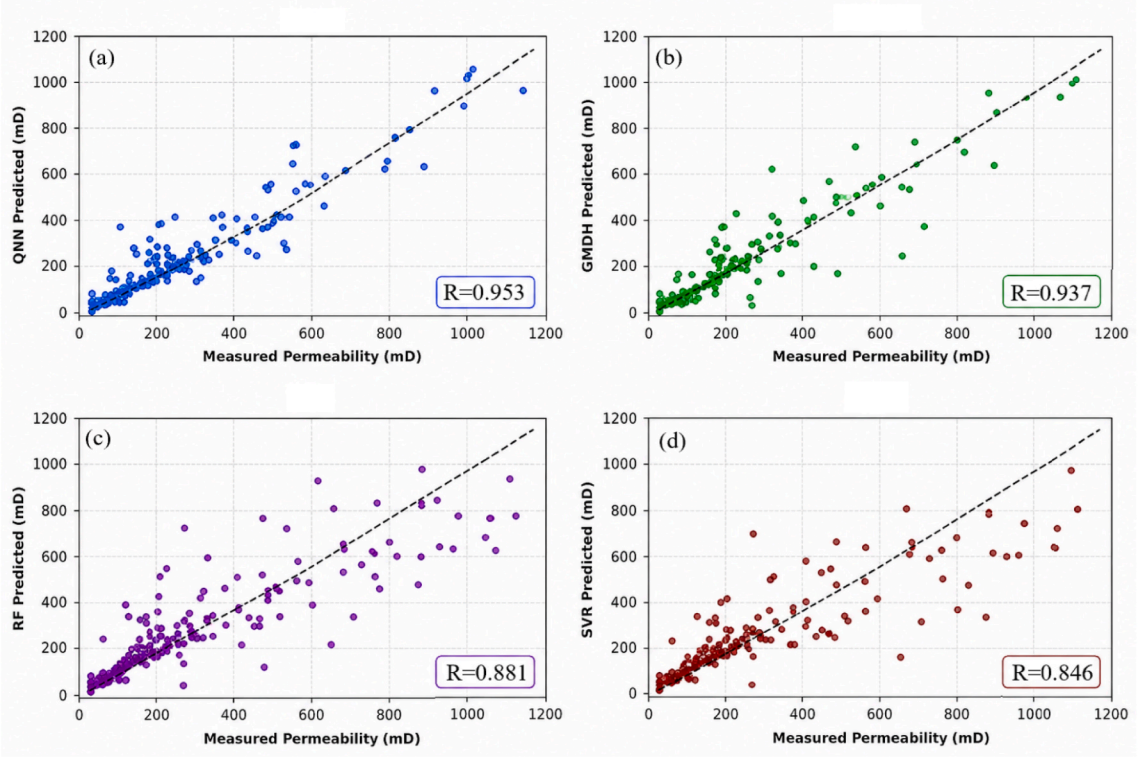

Fig. 10. Comparison between measured and predicted permeability (mD) values during the testing phase (a) QNN, (b) GMDH, (c) RF and (d) SVR.

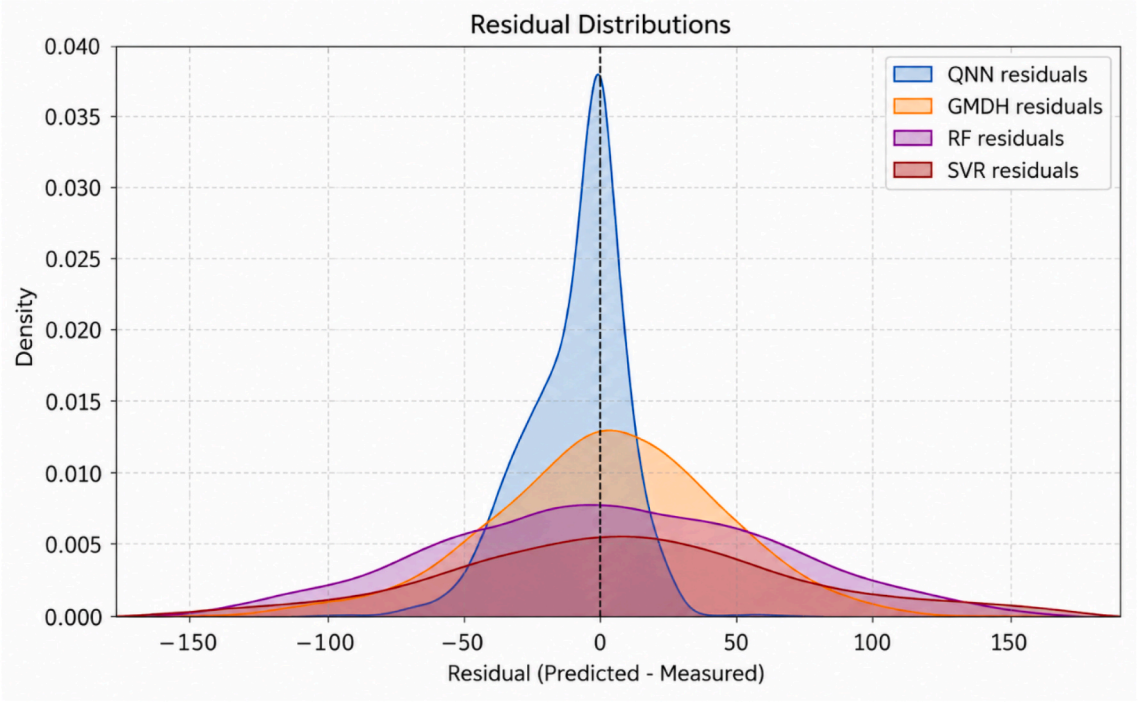

Fig. 11. Comparison of residuals for measured and predicted permeability (mD) for QNN and GMDH models.

This structure selection yields two tangible benefits, lower error because the network concentrates capacity on the signal rather than noise, and greater coherence because redundant or unstable components are removed, reducing overfitting and improving generalization. By contrast, the GMDH approach, while capable of building polynomial relationships, can accumulate more redundant terms or become biased in very low permeabilities, where small absolute differences translate into large relative errors. The RF model demonstrates improved robustness over conventional regression techniques by aggregating predictions from multiple decision trees; however, its ensemble averaging smooths local variations and reduces its ability to accurately reproduce extreme permeability values. This effect becomes more

pronounced in high-permeability intervals, where RF predictions increasingly deviate from the measured values, indicating a compromise between variance reduction and predictive precision. Similarly, the SVR model captures the overall permeability trend but exhibits greater deviations throughout the dataset, especially for samples with moderate-to-high permeability. Its reliance on a fixed kernel function limits its capacity to fully represent the highly nonlinear relationship between well log responses and reservoir permeability, leading to both underestimation of permeability peaks and overestimation of some lower permeability intervals. The comparative figures of measured versus predicted permeability illustrate these dynamics for the training data set, as shown in Fig. 12, and for the testing data set in Fig. 13.

4.3. Blocked five-fold cross-validation performance

The predictive performance of the QNN, GMDH, RF, and SVR models was evaluated using blocked five-fold cross-validation, in which each validation fold consisted of a contiguous depth interval rather than randomly selected samples. Table 6 shows the corresponding depth interval for each validation block, indicating that the validation process maintains the spatial continuity of the well-log measurements and reduces the information leakage due to depth autocorrelation. This validation approach gives rigorous validation of the model across independent depth intervals in the reservoir.

The QNN consistently had the highest predictive accuracy, with the correlation coefficient ranging from 0.982 to 0.989 (mean R = 0.985), RMSE values from 0.029 to 0.034, and MAE values from 0.016 to 0.019. The relatively small difference in performance between the validation blocks suggests that the QNN has a consistent predictive performance for various reservoir intervals, even if the lithology and petrophysical properties vary. The results show that the variational quantum circuit successfully captures the complex nonlinear relationships between well-log measurements and reservoir permeability, and has robust predictive behavior across the study interval.

The GMDH model also showed relatively consistent performance across the five validation blocks, although the predictive accuracy was not as high as that of the QNN. Correlation coefficients ranged from 0.931 to 0.946 (mean R = 0.939), while RMSE and MAE varied between 0.064–0.072 and 0.036–0.041, respectively. The larger dispersion of the validation blocks as compared with the QNN indicates that the sensitivity of the polynomial-based architecture is more to variation in reservoir heterogeneity and lithological variability.

There was a progressive decline in predictive performance for the RF and SVR models across the blocked validation procedure. The RF model was moderately predictive with a mean correlation coefficient of 0.904, a mean RMSE of 0.094 and a mean MAE of 0.054, suggesting reasonable generalization among the various depth blocks. The SVR model had the lowest overall predictive accuracy, with a mean correlation coefficient of 0.861, a mean RMSE of 0.124, and a mean MAE of 0.074, as it was the one that was the least able to model the highly nonlinear relationships governing permeability variations within the reservoir.

Overall, the blocked cross-validation results prove that the proposed QNN can consistently achieve the best predictive accuracy and the least prediction error for the five independent depth intervals across all models evaluated. The relative fold-to-fold variation is also relatively small and supports the robustness of QNN to estimate reservoir permeability under variable geological conditions.

4.4. SHapley additive ExPlanation (SHAP)

Feature selection is an integral component of the proposed predictive framework, as it directly influences the model's ability to accurately predict reservoir permeability. The process begins with the extraction of relevant features from well log data, which serves as the primary input for the predictive model. SHapley Additive exPlanations (SHAP) are utilized to quantify the importance of individual features within the dataset. SHAP values provide a measure of each feature's contribution to the model's predictions, offering insights into their relative significance. By combining QNNs with SHAP, this framework achieves a dual objective, enhancing prediction accuracy through optimal feature representation and improving interpretability by identifying key factors influencing permeability (Belhouchet et al., 2021; Li et al., 2025). SHAP values were computed using KernelExplainer, a model-agnostic approximation of Shapley values suitable for the QNN's non-differentiable simulated-circuit output, applied to the Well-3 blind test set to evaluate feature attributions under genuine out-of-sample generalization rather than training-set fit, using a random subsample of 100 training set as the background reference distribution.

The SHAP summary bar plot (Fig. 14) quantitatively illustrates the relative contribution of each input feature to the Permeability prediction model by presenting their mean absolute SHAP values. PHIE stands out as the most influential parameter, with a mean SHAP value of approximately 150, clearly demonstrating its dominant role in influencing the model's output. This strong influence is consistent with its geological

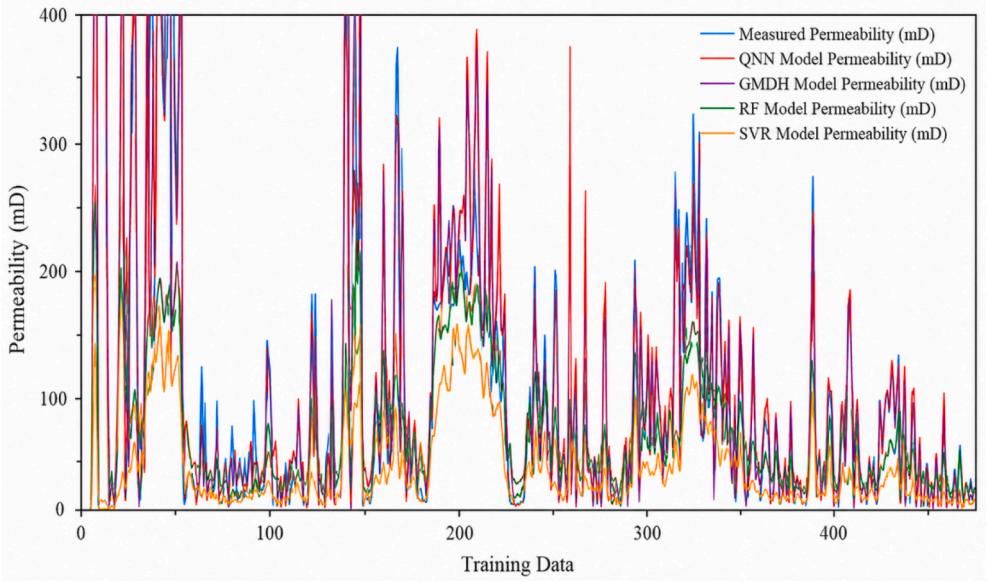

Fig. 12. Comparison of predicted permeability values of QNN, GMDH, RF and SVR with actual permeability (mD) for the training data set.

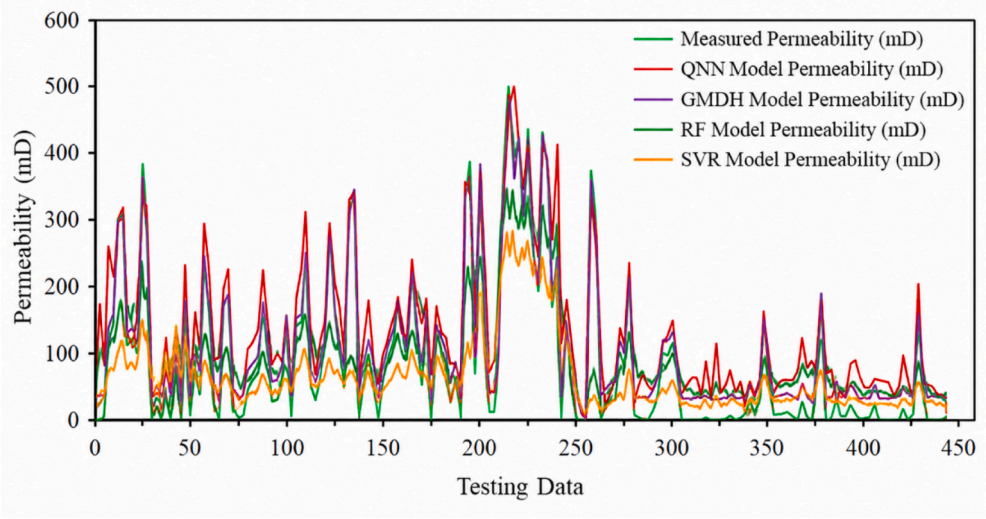

Fig. 13. Comparison of predicted permeability values of QNN, GMDH, RF and SVR with actual permeability (mD) for the testing data set.

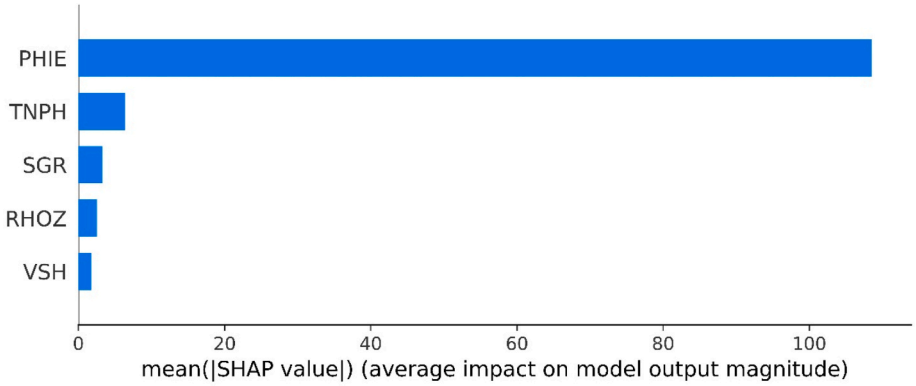

Fig. 14. The SHAP summary bar plot for feature importance.

significance, as higher PHIE values often correspond to increased porosity and improved fluid flow characteristics in the reservoir. TNPH and SGR follow with nearly equal mean SHAP values of around 15 each, indicating that they contribute comparably and substantially to the predictions. RHOZ and VSH show smaller contributions, with mean SHAP values of about 8 and 5, respectively, reflecting their secondary but still relevant roles. These differences in magnitude emphasize the varying sensitivities of the model to different petrophysical logs, with PHIE, TNPH, and SGR providing the most geologically robust signals for permeability estimation.

The SHAP beeswarm plot (Fig. 15) offers an instance-level perspective on feature influence by displaying the distribution of SHAP values across all samples. For PHIE, high values (depicted in red) strongly increase predicted Permeability, with SHAP values reaching more than

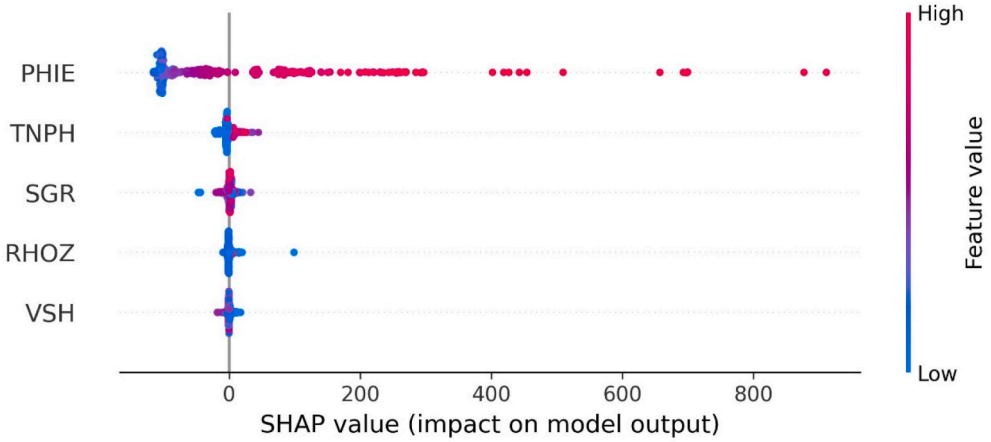

Fig. 15. SHAP beeswarm plot illustrating the influence of well log features.

+800mD, while low values (blue) decrease predictions, sometimes down to −35mD. This asymmetrical pattern reinforces the consistent positive relationship between porosity and Permeability. TNPH exhibits a similar positive trend, where higher readings increase SHAP values up to about +60mD, supporting its role as a proxy for hydrocarbon saturation. SGR shows a more balanced influence, with both high and low values affecting predictions in either direction, although most SHAP values remain within the ±50mD to +100mD range. RHOZ and VSH have less pronounced effects, with most SHAP values within ±50, suggesting their contributions are more context-dependent and often act in synergy with other features.

The SHAP waterfall plot (Fig. 16) focuses on a single prediction to break down the additive contributions of individual features toward the final Permeability estimation. In Fig. 16, the model's expected baseline output is 6.85mD, while the final predicted value is 127.59mD. TNPH contributes the largest positive shift of +7.41, making it the most impactful feature in the prediction. This step-by-step decomposition confirms how specific petrophysical conditions, such as neutron porosity, drive model outputs and offers geological clarity on the interplay of reservoir Permeability at the sample level. Such interpretability strengthens confidence in the model's predictive reliability and its alignment with subsurface geological principles.

To further investigate the influence of individual petrophysical variables, SHAP dependence plots were generated for the most influential predictors. Unlike the SHAP summary plot, dependence plots reveal how changes in each feature affect the predicted permeability while simultaneously illustrating interactions with other variables. The dependence plot of effective porosity (PHIE) demonstrates a clear positive relationship with permeability. As PHIE increases, the corresponding SHAP values become progressively larger, indicating that greater pore volume contributes positively to permeability prediction as shown in Fig. 17 (a). This behavior is consistent with established petrophysical principles, where larger interconnected pore networks facilitate fluid flow through the reservoir [68]. Conversely, shale volume (VSH) exhibits predominantly negative SHAP values at higher concentrations, indicating that increasing clay content reduces predicted permeability as shown in Fig. 17 (b). This trend reflects the pore-blocking effect of clay minerals and the reduction of effective pore throat connectivity. Thermal neutron porosity (TNPH) shows a nonlinear relationship with permeability, suggesting that its contribution depends on interactions with other reservoir properties such as porosity and shale content as shown in Fig. 17 (c).

4.5. Sensitivity analysis results

The CASI results revealed that PHIE is the most influential feature, followed by TNPH and SGR, while RHOZ and VSH contributed comparatively less, as displayed in Table 7. This feature-ranking order was fully consistent with SHAP-derived rankings. The agreement between CASI and SHAP demonstrates that both global and local interpretability techniques converge toward the same understanding of feature influence.

The alignment between CASI and SHAP confirms that the QNN model is driven by geologically meaningful patterns and is not overfitting to noise or spurious correlations. PHIE's leading role is consistent with pore-connectivity control on permeability, whereas TNPH and SGR reflect porosity-fluid sensitivity and clay-related effects, respectively.

4.6. Uncertainty quantification

To further evaluate the reliability of the proposed QNN, bootstrap resampling was employed to estimate prediction uncertainty for the blind test well. In addition to constructing 95% prediction intervals, the quality of the uncertainty estimates was quantified using the Prediction Interval Coverage Probability (PICP) and the Mean Prediction Interval Width (MPIW).

The Prediction Interval Coverage Probability is defined as

$$PICP = \frac{1}{N}\sum_{i=1}^{N} I(L_i \le y_i \le U_i) \tag{26}$$

where N denotes the total number of blind-test samples, L_i and U_i represent the lower and upper prediction limits, respectively, y_i is the measured permeability, and $I(\cdot)$ is the indicator function.

The average width of the prediction intervals is calculated as

$$MPIW = \frac{1}{N}\sum_{i=1}^{N} (U_i - L_i) \tag{27}$$

where narrower intervals indicate greater predictive precision while maintaining adequate coverage.

Uncertainty in the QNN permeability predictions was assessed using a 30-member bootstrap ensemble: each ensemble member was trained on a resampled (with replacement) draw from the training set, and 95% prediction intervals were constructed from the 2.5th and 97.5th percentiles of the resulting predictive distribution at each test point. Evaluated on the blind test well, the intervals achieved an empirical coverage (PICP) of 91.01% against a 95% nominal target, with a mean interval width (MPIW) of 70.56 mD. Table 8 summarizes the 95% prediction intervals over four 100 m depth intervals across the blind well (1200–1600 m). Interval widths were narrowest in the 1500–1600 m interval (15.6 mD), corresponding to the lowest mean gamma-ray response and shale volume in the well, and widest in the

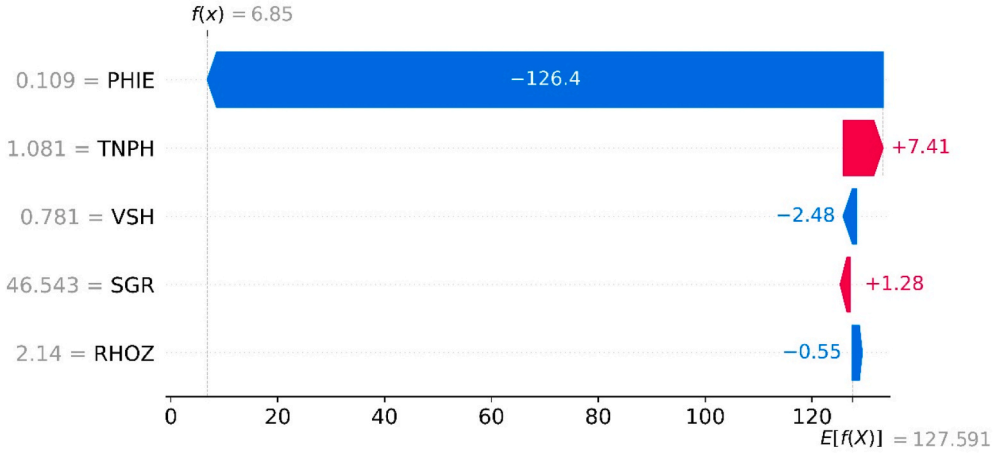

Fig. 16. The SHAP waterfall plot for additive contributions of each feature toward the Permeability prediction.

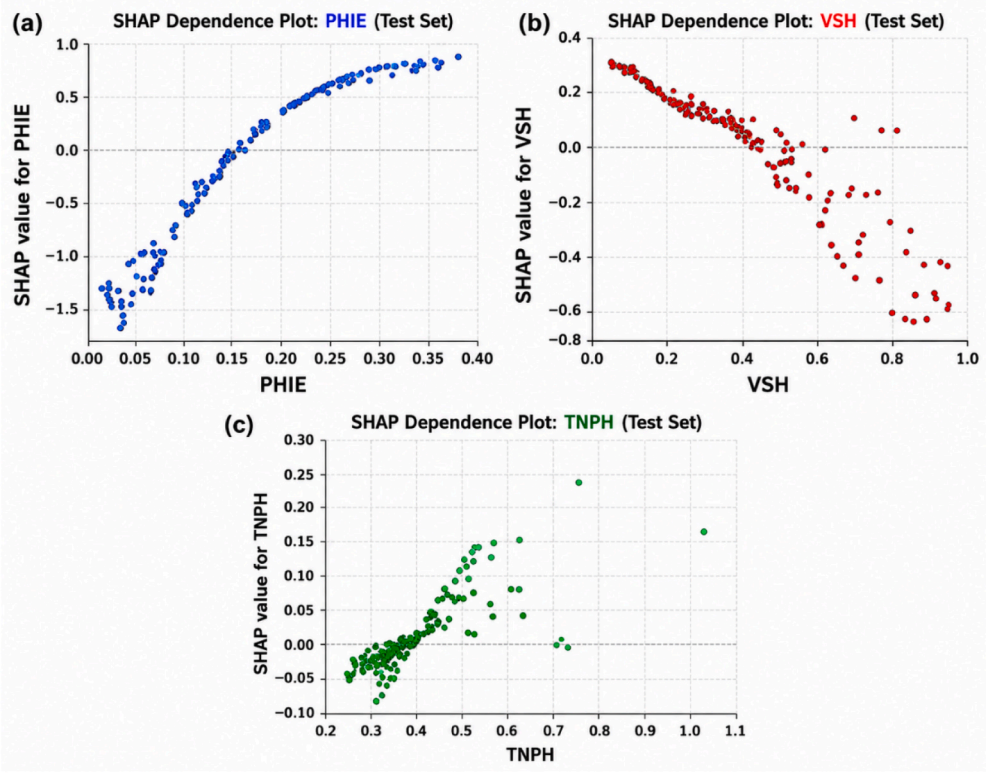

Fig. 17. SHAP dependence plot for (a) PHIE (b) VSH and (c) TNPH.

Table 6
Performance of blocked five-fold cross-validation using contiguous depth intervals for the QNN, GMDH, RF, and SVR models.

Validation Block	Depth Interval (m)	QNN			GMDH			RF			SVR		
		R	RMSE	MAE	R	RMSE	MAE	R	RMSE	MAE	R	RMSE	MAE
Block 1	1200-1280	0.989	0.029	0.016	0.946	0.064	0.036	0.912	0.091	0.051	0.869	0.12	0.071
Block 2	1280-1360	0.984	0.033	0.018	0.938	0.071	0.04	0.901	0.098	0.056	0.858	0.127	0.076
Block 3	1360-1440	0.982	0.034	0.019	0.931	0.072	0.041	0.895	0.099	0.057	0.853	0.129	0.078
Block 4	1440-1520	0.988	0.03	0.017	0.944	0.066	0.037	0.909	0.093	0.052	0.865	0.122	0.072
Block 5	1520-1600	0.984	0.031	0.018	0.936	0.068	0.038	0.902	0.091	0.053	0.86	0.123	0.073
Mean		0.985	0.031	0.018	0.939	0.068	0.038	0.904	0.094	0.054	0.861	0.124	0.074

Table 7
Global sensitivity ranking using the cosine-amplitude sensitivity index (CASI).

Feature	CASI Value	Sensitivity Rank
PHIE	0.92	1
TNPH	0.75	2
SGR	0.63	3
RHOZ	0.41	4
VSH	0.35	5

1300–1400 m interval (119.1 mD), where permeability itself is highest and log responses are most variable. Across all test points, interval width correlated positively with both SGR ($r = 0.42$) and VSH ($r = 0.69$), confirming that the QNN's uncertainty estimates widen systematically in clay-rich, heterogeneous intervals rather than behaving uniformly across the well. This is consistent with reduced log sensitivity and greater pore-scale structural variability in shaly facies. The near-nominal (91% vs. 95% target) coverage indicates the bootstrap ensemble is reasonably well-calibrated, with residual undercoverage concentrated in a small number of very-low-permeability points near the detection floor of the log suite.

Bootstrap-based uncertainty analysis indicated that the QNN produced narrow 95% prediction intervals in clean, sand-rich intervals, reflecting high predictive confidence. Wider prediction intervals were observed in clay-rich or heterogeneous zones characterized by elevated SGR and VSH values as shown in Fig. 18. The widening of uncertainty

Table 8
95% prediction intervals for QNN permeability predictions based on bootstrap resampling.

Depth Interval (m)	N	Mean Permeability (mD)	Lower U95	Upper U95	Interval Width (mD)	Coverage (%)
1200–1300	45	86.9	64.7	131.2	66.4	93.33
1300–1400	44	134.3	99.8	219.0	119.1	97.73
1400–1500	44	85.7	64.2	146.6	82.4	88.64
1500–1600	45	20.2	14.6	30.2	15.6	84.09
Overall					MPIW = 70.56	PICP = 91.01%

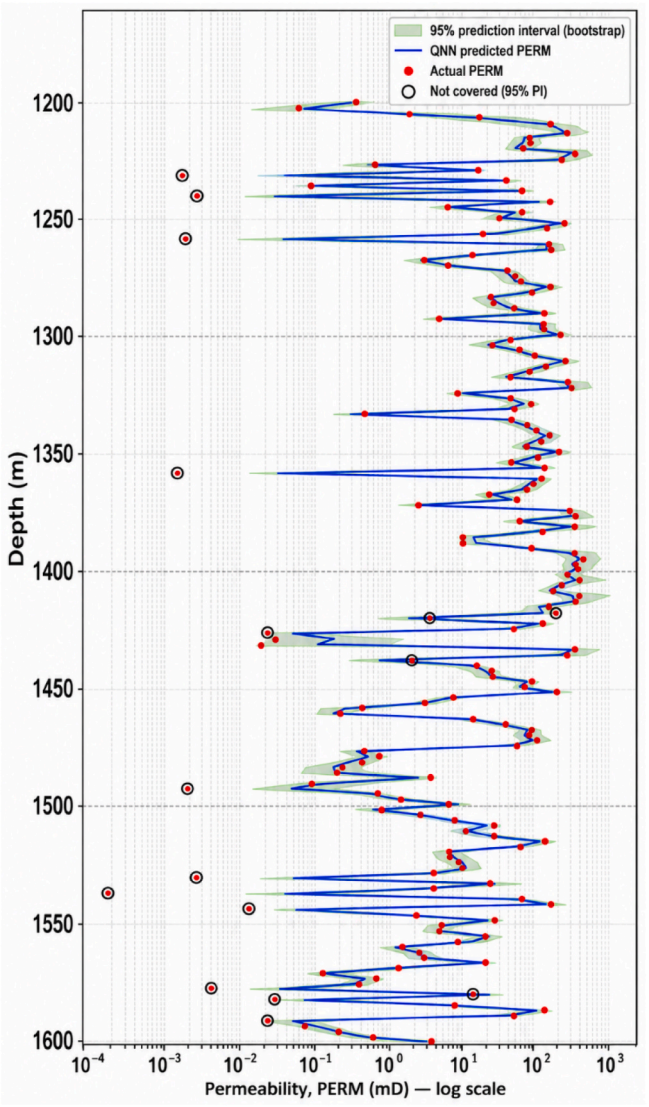

Fig. 18. Predicted permeability with 95% bootstrap prediction intervals versus depth along the blind test well.

bands in these zones suggests increased subsurface complexity, reduced log sensitivity, and greater structural variability at the pore scale [69]. Overall, the UQ results confirm that the QNN not only provides improved predictive accuracy but also offers well-behaved and geologically consistent uncertainty estimates.

5. Conclusion

The advancements in predicting reservoir permeability through innovative methodologies signify a transformative shift in the field of oil and gas exploration. The integration of machine learning techniques, particularly Quantum Neural Networks (QNNs) combined with SHapley Additive exPlanations (SHAP), has demonstrated substantial improvements in both accuracy and interpretability. These approaches effectively address the limitations of traditional methods, which often oversimplify complex geological formations and fail to capture the intricate relationships between various well log as influencing factors. By leveraging high-dimensional data and sophisticated modeling techniques, a more reliable prediction of permeability in heterogeneous reservoirs can now be achieved. The ability of QNNs to process complex well log datasets while maintaining computational efficiency is particularly noteworthy, as it allows for the analysis of well log data that is often altered by geological complexities. This capability not only enhances prediction accuracy but also provides valuable insights into the underlying mechanisms driving fluid flow behavior.

Despite the promising results, the study is constrained by the limited number of wells (three) and the specific depositional environment of the Mpyo Field. The resulting dataset, while sufficient for model development, may not encapsulate the full range of heterogeneity found in other basins or reservoir types. Future work should therefore incorporate additional wells, extend the dataset across broader stratigraphic and lithological contexts, and evaluate model transferability to shale reservoirs or unconventional systems using expanded input features such as NMR or micro resistivity measurements.

Furthermore, the application of interpretability tools such as SHAP facilitates a deeper understanding of how specific well log features, such as effective porosity (PHIE), standard resolution formation density (RHOZ), and shale volume (VSH), influence permeability predictions. This transparency is crucial for informed decision making in reservoir management, enabling operators to optimize drilling plans and production strategies while minimizing environmental impacts. As the field continues to evolve, the integration of advanced machine learning algorithms will be essential in addressing the complexities associated with reservoir heterogeneity. Ultimately, by embracing these innovative approaches, this study is paving the way for more effective and interpretable solutions tailored to the challenges of modern energy production. The ongoing development and refinement of these methodologies will play a critical role in shaping the future of reservoir permeability prediction and ensuring sustainable energy practices.

CRediT authorship contribution statement

Alvin K. Mulashani: Writing – original draft, Supervision, Software, Methodology, Conceptualization. **Christopher N. Mkono:** Writing – review & editing, Formal analysis, Data curation. **Melckzedeck M. Mgimba:** Methodology, Validation. **Grant Charles Mwakipunda:** Software, Validation, Writing – review & editing.

Data and code availability

Data and code used in this study can be made available upon request to the corresponding author.

Declaration of competing interest

The authors declare that they have no known competing financial interests or personal relationships that could have appeared to influence the work reported in this paper.

Nomenclature

PHIE	Effective porosity (%)
TNPH	Thermal neutron porosity (v/v)
RHOZ	Formation density (g/cm^3)
SGR	Spectral gamma ray (API)
VSH	Shale volume (pU)
k	Permeability (mD)
RMSE	Root Mean Square Error
MAE	Mean Absolute Error
R	Correlation coefficient
QNN	Quantum Neural Network
GMDH	Group Method of Data Handling
SHAP	SHapley Additive exPlanations
ML	Machine Learning
UQ	Uncertainty Quantification
CV	Cross-validation

References

[1] M. Bilgili, S. Tumse, S. Nar, Comprehensive overview on the present state and evolution of global warming, climate change, greenhouse gasses and renewable energy, Arabian J. Sci. Eng. 49 (11) (2024) 14503–14531.

[2] C.N. Mkono, C. Shen, A.K. Mulashani, P. Nyangi, An improved permeability estimation model using integrated approach of hybrid machine learning technique and shapley additive explanation, J. Rock Mech. Geotech. Eng. 17 (5) (2025) 2928–2942.

[3] A.K. Mulashani, C. Shen, B.M. Nkurlu, C.N. Mkono, M. Kawamala, Enhanced group method of data handling (GMDH) for permeability prediction based on the modified levenberg marquardt technique from well log data, Energy 239 (2022) 121915.

[4] G.C. Mwakipunda, et al., Underground hydrogen storage in geological formations: a review, J. Rock Mech. Geotech. Eng. (2025).

[5] A. Lawal, Y. Yang, H. He, N.L. Baisa, Machine learning in oil and gas exploration: a review, IEEE Access 12 (2024) 19035–19058.

[6] B. Mathew Nkurlu, et al., Prediction of permeability using group method of data handling (GMDH) neural network from well log data, Energies 13 (3) (2020) 551.

[7] R. Peng, X. Yang, Recent advances in the application of porosity and permeability in porous media, Phys. Fluids 37 (7) (2025).

[8] A. Sheykhinasab, et al., Prediction of permeability of highly heterogeneous hydrocarbon reservoir from conventional petrophysical logs using optimized data-driven algorithms, J. Pet. Explor. Prod. Technol. 13 (2) (2023) 661–689.

[9] R. Ahmed, G.M. Farman, How to estimate the major petrophysical properties: a review, Iraqi Journal of Oil and Gas Research (IJOGR) 3 (1) (2023) 43–58.

[10] C.F. Haro, Permeability modeling in porous media: setting archie and carman-kozeny right. SPE International Oil Conference and Exhibition in Mexico. SPE, 2007. SPE-100201-MS.

[11] A.K. Mulashani, C. Shen, S. Asante-Okyere, P.N. Kerttu, E.N. Abelly, Group method of data handling (GMDH) neural network for estimating total organic carbon (TOC) and hydrocarbon potential distribution (S1, S2) using well logs, Nat. Resour. Res. 30 (5) (2021) 3605–3622.

[12] Y. Wei, X. Xue, Permeability prediction in tight carbonate rocks using gene expression programming (GEP), Rock Mech. Rock Eng. 54 (5) (2021) 2581–2593.

[13] C.N. Mkono, et al., Improved reservoir porosity estimation using an enhanced group method of data handling with differential evolution model and explainable artificial intelligence, SPE J. (2025) 1–19.

[14] Y. Zhen, et al., Prediction of deep low permeability sandstone seismic reservoir based on CBAM-CNN, Geoenergy Sci. Eng. 242 (2024) 213241.

[15] Y. Zhou, S.-T. Wu, R.-K. Zhu, X.-H. Jiang, G.-L. Hua, A new model for determining the effective permeability of tight reservoirs based on fractal-monte carlo method, Pet. Sci. (2025).

[16] A.F. Ibrahim, Advanced generalized machine learning models for predicting hydrogen–brine interfacial tension in underground hydrogen storage systems, Sci. Rep. 15 (1) (2025) 18972.

[17] J. Lai, Y. Su, L. Xiao, F. Zhao, T. Bai, Y. Li, H. Li, Y. Huang, G. Wang, Z. Qin, Application of geophysical well logs in solving geologic issues: past, present and future prospect, Geosci. Front. 15 (3) (2024) 101779.

[18] M.A. Abbas, W.J. Al-Mudhafar, D.A. Wood, Improving permeability prediction in carbonate reservoirs through gradient boosting hyperparameter tuning, Earth Sci. Inf. 16 (4) (2023) 3417–3432.

[19] N. Alizadeh, N. Rahmati, A. Najafi, E. Leung, P. Adabnezhad, A novel approach by integrating the core derived FZI and well logging data into artificial neural network model for improved permeability prediction in a heterogeneous gas reservoir, J. Petrol. Sci. Eng. 214 (2022) 110573.

[20] M. Masroor, M.E. Niri, M.H. Sharifinasab, A multiple-input deep residual convolutional neural network for reservoir permeability prediction, Geoenergy Sci. Eng. 222 (2023) 211420.

[21] A.K. Mulashani, E.N. Abelly, Novel material balance approach for estimating shale gas reserves with carbon dioxide (CO_2) enhanced recovery, Carbonates Evaporites 41 (1) (2026) 10.

[22] M.K. Elshaarawy, M. Zeleňáková, A.M. Armanuos, Hydraulic performance modeling of inclined double cutoff walls beneath hydraulic structures using optimized ensemble machine learning, Sci. Rep. 15 (1) (2025) 27592.

[23] F. Yu, H.F. Isleem, W.J. Almoghayer, R.I. Shahin, S.A. Yehia, M. Khishe, M. K. Elshaarawy, Predicting axial load capacity in elliptical fiber reinforced polymer concrete steel double skin columns using machine learning, Sci. Rep. 15 (1) (2025) 12899.

[24] X. Liu, D. Zhang, T. Zhang, J. Zhang, J. Wang, A new path plan method based on hybrid algorithm of reinforcement learning and particle swarm optimization, Eng. Comput. 39 (3) (2022) 993–1019.

[25] R. Rezaee, J. Ekundayo, Permeability prediction using machine learning methods for the CO2 injectivity of the precipice sandstone in surat basin, Australia, Energies 15 (6) (2022) 2053.

[26] M. Matinkia, R. Hashami, M. Mehrad, M.R. Hajsaeedi, A. Velayati, Prediction of permeability from well logs using a new hybrid machine learning algorithm, Petroleum 9 (1) (2023) 108–123.

[27] M.M. Alsaadawi, M.K. Elshaarawy, A.K. Hamed, Concrete compressive strength classification using hybrid machine learning models and interactive GUI, Innov. Infrastruct. Solut. 10 (5) (2025) 1–29.

[28] R. Kalule, H.A. Abderrahmane, W. Alameri, M. Sassi, Stacked ensemble machine learning for porosity and absolute permeability prediction of carbonate rock plugs, Sci. Rep. 13 (1) (2023) 9855.

[29] E. Mohammadian, M. Kheirollahi, B. Liu, M. Ostadhassan, M. Sabet, A case study of petrophysical rock typing and permeability prediction using machine learning in a heterogenous carbonate reservoir in Iran, Sci. Rep. 12 (1) (2022) 4505.

[30] H. Al Khalifah, P. Glover, P. Lorinczi, Permeability prediction and diagenesis in tight carbonates using machine learning techniques, Mar. Petrol. Geol. 112 (2020) 104096.

[31] G. Zhang, et al., Pattern visualization and understanding of machine learning models for permeability prediction in tight sandstone reservoirs, J. Petrol. Sci. Eng. 200 (2021) 108142.

[32] A. Mahdy, W. Zakaria, A. Helmi, A.S. Helaly, A.M. Mahmoud, Machine learning approach for core permeability prediction from well logs in sandstone reservoir, Mediterranean Sea, Egypt, J. Appl. Geophys. 220 (2024) 105249.

[33] J. Ullah, et al., Optimizing support vector machines for enhanced permeability prediction in sandstone reservoirs using systematic and heuristic hyperparameter tuning, Earth Sci. Inf. 18 (1) (2025) 88.

[34] N. Liu, et al., Quantum-enhanced deep learning-based lithology interpretation from well logs, IEEE Trans. Geosci. Rem. Sens. 60 (2021) 1–13.

[35] D. Luo, Y. Liang, Y. Yang, X. Wang, Hybrid parameters for fluid identification using an enhanced quantum neural network in a tight reservoir, Sci. Rep. 14 (1) (2024) 1064.

[36] C.J. Nicholas, Chapter 9. Albertine rift stratigraphy 1: sedimentary architecture, Geological Society, London, Memoirs 61 (1) (2025). M61-2024-62.

[37] K. Teddy, An Analysis of the Effects of Oil and Gas Exploration on Tourism in the Albertine Region, Institute of Petroleum Studies-Kampala, 2021.

[38] D. Abeinomugisha, P. Obita, Petroleum Exploration and Development in a Frontier, Remote Rift Basin: the Albertine Graben of the East African Rift System, 2011.

[39] D. Lirong, et al., Geological conditions and petroleum exploration potential of the albertine graben of Uganda, Acta Geol. Sin. Engl. Ed. 78 (4) (2004) 1002–1010.

[40] A.B. Katumwehe, M.G. Abdelsalam, E.A. Atekwana, The role of pre-existing Precambrian structures in rift evolution: the Albertine and Rhino grabens, Uganda, Tectonophysics 646 (2015) 117–129.

[41] A.B. Katumwehe, The Role of Pre-existing Precambrian Structures and Thermal Anomaly in Rift Initiation and evolution-the Albertine and Rhino Grabens in Uganda, Oklahoma State University, 2016.

[42] F.U. Bauer, U.A. Glasmacher, U. Ring, A. Schumann, B. Nagudi, Thermal and exhumation history of the central Rwenzori Mountains, Western rift of the east African rift system, Uganda, Int. J. Earth Sci. 99 (7) (2010) 1575–1597.

[43] S. Schneider, J. Hornung, M. Hinderer, Evolution of the western East African Rift system reflected in provenance changes of Miocene to Pleistocene synrift sediments (Albertine Rift, Uganda), Sediment. Geol. 343 (2016) 190–205.

[44] S. Mutebi, et al., Geological characterization of the Miocene–Pliocene succession in the semliki basin, Uganda: implications for hydrocarbon exploration and drilling in the east African Rift System, Nat. Resour. Res. 30 (6) (2021) 4329–4354.

[45] S. Roller, J. Hornung, M. Hinderer, I. Ssemmanda, Middle Miocene to Pleistocene sedimentary record of rift evolution in the southern Albert Rift (Uganda), Int. J. Earth Sci. 99 (7) (2010) 1643–1661.

[46] W.J. Al-Mudhafar, A.A. Hasan, M.A. Abbas, D.A. Wood, Machine learning with hyperparameter optimization applied in facies-supported permeability modeling in carbonate oil reservoirs, Sci. Rep. 15 (1) (2025) 12939.

[47] A. Mehrabi, M. Bagheri, M. Nabi Bidhendi, E. Biniaz Delijani, M. Behnood, Enhancing porosity prediction accuracy in oil reservoirs: evaluating hybrid machine learning approaches integrating well log and core data, J. Earth Space Phys. 50 (4) (2025).

[48] E.a. Alshdaifat, D.A. Alshdaifat, A. Alsarhan, F. Hussein, S.M.d.F.S. El-Salhi, The effect of preprocessing techniques, applied to numeric features, on classification algorithms' performance, Data 6 (2) (2021) 11.

[49] V. Çetin, O. Yıldız, A comprehensive review on data preprocessing techniques in data analysis, Pamukkale Üniversitesi Mühendislik Bilimleri Dergisi 28 (2) (2022) 299–312.

[50] G.S. Krishna, K. Supriya, K.M. Rao, Selection of data preprocessing techniques and its emergence towards machine learning algorithms using hpi dataset, in: 2022 IEEE Global Conference on Computing, Power and Communication Technologies (GlobConPT), IEEE, 2022, pp. 1–6.

[51] A. Saleem, K.H. Asif, A. Ali, S.M. Awan, M.A. Alghamdi, Pre-processing methods of data mining, in: 2014 IEEE/ACM 7th International Conference on Utility and Cloud Computing, IEEE, 2014, pp. 451–456.

[52] L. Zhu, X. Zhou, C. Zhang, Rapid identification of high-quality marine shale gas reservoirs based on the oversampling method and random forest algorithm, Artif. Intell. Geos 2 (2021) 76–81.

[53] M. Meng, R. Zhong, Z. Wei, Prediction of methane adsorption in shale: classical models and machine learning based models, Fuel 278 (2020) 118358.

[54] A. Amosu, M. Imsalem, Y. Sun, Effective machine learning identification of TOC-rich zones in the Eagle Ford Shale, J. Appl. Geophys. 188 (2021) 104311, https://doi.org/10.1016/j.jappgeo.2021.104311.

[55] W. Niu, et al., Development of visual prediction model for shale gas wells production based on screening main controlling factors, Energy 250 (2022) 123812, https://doi.org/10.1016/j.energy.2022.123812.

[56] M. Mrugalski, J. Korbicz, GMDH Neural Networks, Intelligent Systems, CRC Press, 2018, 8-1-8-21.

[57] A. Taheri, et al., A fully-self-adaptive harmony search GMDH-type neural network algorithm to estimate shear-wave velocity in porous media, Appl. Sci. 12 (13) (2022) 6339.

[58] M.A. Sattari, M. Hayati, A novel approach to oil-water mixture analysis: microstrip antenna-based sensor combined with GMDH neural network, Flow Meas. Instrum. 101 (2025) 102751.

[59] A.J. Fofanah, Artificial neural network model with adaptive GMDH technique for non-linear regression prediction, Int. J. Sci. Eng. Res. 12 (5) (2021).
[60] M. Caponi, Use of Image-based Machine Learning and Quantum Learning for Subsurface Characterization, 2022.
[61] J. Song, et al., A new method for identifying reservoir fluid properties based on well logging data: a case study from PL block of Bohai Bay Basin, North China, Open Geosci. 16 (1) (2024) 20220716.
[62] Y. Kwak, W.J. Yun, S. Jung, J. Kim, Quantum neural networks: concepts, applications, and challenges, in: 2021 Twelfth International Conference on Ubiquitous and Future Networks (ICUFN), IEEE, 2021, pp. 413–416.
[63] S.K. Suman, S.S. Kamal, A. Kumar, J. Khatti, A. Bardhan, Prediction of CBR of hydrated lime-activated rice husk ash (HARHA) treated soil using genetic and particle swarm optimized ANN, LSSVM, and RVM models, Transportation Infrastructure Geotechnology 12 (6) (2025) 185.
[64] S. Battula, S. Alla, E. Ramana, N.K. Kumar, S.B. Murthy, Uncertainty quantification for digital twins in smart manufacturing and robotics: a review, in: Journal of Physics: Conference Series, vol. 2837, IOP Publishing, 2024 012059.
[65] S. Uddin, I. Haque, H. Lu, M.A. Moni, E. Gide, Comparative performance analysis of K-nearest neighbour (KNN) algorithm and its different variants for disease prediction, Sci. Rep. 12 (1) (2022) 6256.
[66] A. Batool, et al., Assessing the generalization of forecasting ability of machine learning and probabilistic models for complex climate characteristics, Stoch. Environ. Res. Risk Assess. 38 (8) (2024) 2927–2947.
[67] R. Moazenzadeh, B. Mohammadi, Z. Duan, M. Delghandi, Improving generalisation capability of artificial intelligence-based solar radiation estimator models using a bio-inspired optimisation algorithm and multi-model approach, Environ. Sci. Pollut. Control Ser. 29 (19) (2022) 27719–27737.
[68] A.K. Mulashani, N. Mkono Christopher, Early Jurassic successions total organic carbon prediction using Bayesian physics-informed neural network in the mandawa basin, SE Tanzania, SPE J. 31 (6) (2026) 3509–3527.
[69] A.K. Mulashani, Z. Desheng, M. Kawamala, Significance of advanced spontaneous imbibition, and wettability alteration on enhanced oil recovery (EOR) in tight oil reservoirs, in: International Field Exploration and Development Conference, Springer, 2019, pp. 3763–3780.